


Research Article

Climatic and cave settings influence on drip water fluorescent organic matter with implications for fluorescent laminations in stalagmites

Laura Sibylla Endres^a , Céline Jacquin^b, Saúl González-Lemos^c, Laura Rodríguez-Rodríguez^c, Jakub Sliwinski^d, Nikita Kaushal^a, Oliver Kost^a and Heather Marie Stoll^a

^aDepartment of Earth Sciences, ETH Zürich, 8092 Zürich, Switzerland; ^bDepartment of Process Engineering, EAWAG, 8600 Dübendorf, Switzerland; ^cDepartamento de Geología, Universidad de Oviedo, 33005 Oviedo, Spain and ^dSchool of Earth and Environmental Sciences, University of St. Andrews, St. Andrews KY16 9TS, Scotland

Abstract

Speleothem fluorescence can provide insights into past vegetation dynamics and stalagmite chronology. However, its origin and especially the formation of fluorescent laminations in stalagmites are poorly understood. We conducted a year-long monthly monitoring of drip water fluorescence in La Vallina Cave (northern Iberian Peninsula) and compared the results to drip water chemistry and active speleothems from the same sites. Drip waters were analyzed using fluorescence spectroscopy and parallel factor analysis (PARAFAC). The resulting five-component model indicates contributions from vegetation, microbial activity, and bedrock. Intra-site fluorescence variability is mainly influenced by changes in overlying vegetation, water reservoir time, and respiration rates. Contrary to prevailing views, we find no systematic increase in drip water fluorescence during rainy conditions across drip sites and seasonal variations in drip water fluorescence are absent at a location where present-day speleothem layers form. Our findings challenge the notion of a higher abundance of humic-like fluorescence during the rainy season as the primary cause for layer formation and suggest additional controls on drip water fluorescence, such as bedrock interaction and microbial reprocessing. We also propose that growth rate may control the dilation of the fluorescence signal in stalagmites, indicating other potential mechanisms for fluorescent layer formation.

Keywords: Banding, Speleothem, Monitoring, Karst aquifer, Climate reconstruction, Proxy development, PARAFAC, Spectrofluorometer, Absorbance, EEM

INTRODUCTION

Fluorescence due to the presence of dissolved organic matter (DOM) has been commonly reported in secondary calcium carbonates found in caves (speleothems) and has been recognized for many decades (O'Brien, 1956). Natural DOM incorporation into calcite depends primarily on water DOM content, according to laboratory precipitation experiments using peat waters (Pearson et al., 2020). Speleothem fluorescence has been characterized by dissolving the organics from the stalagmite matrix (Pearson et al., 2020) and by surface scan in-situ analysis (Perrette et al., 2005). Patterns in the in-situ distribution of fluorescence intensities in a stalagmite have been studied in thin or thick sections using UV excitation and detection on photographic film (Shopov et al., 1994), epifluorescence microscopes (Baker et al., 1993; Luetscher et al., 2021), fibre-optics extensions connected to spectrofluorometer (McGarry and Baker, 2000), a pulsed laser of a fixed wave length (Quiers et al., 2015), and

confocal laser scanning microscopy (CLSM) (Sliwinski and Stoll, 2021).

From in-situ techniques, fine-scale alternations (5–1000 μm) of high- and low-fluorescence intensity perpendicular to the growth axis, have been described from many stalagmites of mid-latitude regions and this layering (“lamination”) has been demonstrated to be annual in many cases (McGarry and Baker, 2000; Proctor et al., 2000; Baker et al., 2008; Luetscher et al., 2021; Sliwinski and Stoll, 2021; Kwiczen et al., 2022). The fine-scale fluorescent intensity variations in some cases exhibit relationships with speleothem trace element chemistry (Huang et al., 2001; Sliwinski et al., 2023). In stalagmites featuring fine-scale alternations of fluorescence, several authors suggested that the seasonal peak in fluorescence intensity is due to an increased influx of DOM in drip waters during increased autumn leaf litter and rainfall (McGarry and Baker, 2000; Borsato et al., 2007; Kwiczen et al., 2022), or alternately due to fine soil blown into the cave as an aerosol (Fairchild and Baker, 2012; Luetscher et al., 2021). In addition to changes in DOM input, changes in adsorption behavior at the crystal level, induced by variations in environmental and cave conditions such as pH, redox state, and cave ventilation, could also cause variations in the incorporation of the fluorescent DOM (Ramseyer et al., 1997; Sliwinski and Stoll,

Corresponding author: Laura Sibylla Endres: Email endres@erdw.ethz.ch

Cite this article: Endres LS, Jacquin C, González-Lemos S, Rodríguez-Rodríguez L, Sliwinski J, Kaushal N, Kost O, Stoll HM (2024). Climatic and cave settings influence on drip water fluorescent organic matter with implications for fluorescent laminations in stalagmites. *Quaternary Research* 118, 41–61. <https://doi.org/10.1017/qua.2023.41>

© The Author(s), 2023. Published by Cambridge University Press on behalf of Quaternary Research Center. This is an Open Access article, distributed under the terms of the Creative Commons Attribution licence (<http://creativecommons.org/licenses/by/4.0/>), which permits unrestricted re-use, distribution and reproduction, provided the original article is properly cited.



2021). Where the processes driving fluorescent layers can be demonstrated to be annual, then fluorescent banding can be exploited as a paleo-seasonality indicator (Ramseyer *et al.*, 1997; Blyth *et al.*, 2008; Orland *et al.*, 2012; Sliwinski and Stoll, 2021). Further, age models potentially can be improved through fluorescent layer counting, although complications arise if multiple (intra-annual) bands form (e.g., due to the repeated flushing of organic matter from the soil [Kwiecien *et al.*, 2022]). However, due to the limited number of monitoring studies and laboratory experiments available, direct evidence for fluorescent banding formation is sparse and the physical process leading to layer formation is currently not understood in detail.

Speleothem and drip water organics originate from surface vegetation (e.g., lignin macromolecules), animal byproducts, and soil processes; but also from biofilms and microbes living in the karst environment (McGarry and Baker, 2000; Fairchild and Baker, 2012). In a carbonate aquifer, organic matter can be degraded by microbial metabolism (Xia *et al.*, 2022) or abiotically through adsorption on the bedrock. In lab experiments by Jin and Zimmermann (2010), DOM adsorption on carbonate host rock was enhanced during times of high influx and long water retention. Jin and Zimmermann (2010) also showed that adsorption acts similar to a “buffer” because organics covering the active crystal surfaces have been shown to inhibit bedrock leaching, but in contrast, low concentrations of DOM in the carbonate aquifer led to a release of indigenous organic matter from the host rock. Further beaker growth experiments indicate that the presence of organic matter in the drip water can alter the fabric of the precipitated carbonates and precipitation kinetics (Pearson *et al.*, 2020). The chemical structure of the organic matter also influences inorganic colloid coagulation (Wilkinson *et al.*, 1997), and subsequently affects the associated trace element transport through the aquifer and incorporation into the calcite matrix (Blyth *et al.*, 2008), especially for first-row transition metals (Lindeman *et al.*, 2021).

Only a minor part of the total DOM incorporated in speleothem fluoresces, often associated with aromatic ring structures (Aiken, 2014). Fluorescence occurs due to a three-step process: (1) a molecule is excited to a higher electronic state by photon absorption; (2) the molecule relaxes to the lowest excited singlet state (vibrational relaxation); and (3) the molecule returns to ground state via light emission (Lakowicz, 2006). The total fluorescence yield depends on molecular structure and rises with increasing structural rigidity (Reynolds, 2014). Because fluorescence does not directly measure organic molecules but rather the interaction of the functional groups such as aromatic rings with photons, a measurement rarely uniquely identifies the compounds present. Yet, differing categories of fluorescent DOM are preferentially excited by, and emit at, different wavelength ranges (Coble *et al.*, 2014), therefore the technique can be used qualitatively to map the main DOM families present in a sample.

In the liquid phase, such as drip waters or dissolved carbonate, three-dimensional excitation-emission matrices (3D EEM) can be measured with spectrofluorometer to provide characterization of the range of DOM types present and have been used extensively to study fresh and marine waters over the last decades (Coble *et al.*, 2014). Two main categories of fluorescent DOM have been described: (1) humic-like fluorescence, which resembles spectral features of isolated humic and fulvic acids (Alberts and Takács, 2004); and (2) protein-like fluorescence, resembling fluorescence of amino acids (Coble *et al.*, 2014). Humic-like, and the subgroup fulvic-like, fluorescence exhibits a distinctive double

peak with a blurred shape in the EEM’s visible range. This fluorescence is thought to arise primarily from the degradation of terrestrial biomaterial, which usually consists of heavier molecules and encompasses various compounds with slightly variable excitation (Ex) and emission (Em) maxima. Protein-like fluorescence, in contrast, consists of light-weight molecules of rather isolated compounds and is thought to be more microbial in origin. The DOM composition in individual EEMs has been described by their main peaks using the Coble peak nomenclature (Coble *et al.*, 2014), which allows a comparison between different studies because individual peaks with fixed wavelength pairs are named.

Another approach to characterize DOM in natural water has been to use the ratios of the intensity at fixed Ex/Em wavelength pairs (e.g., the fluorescence index; McKnight *et al.*, 2001). More recently, parallel factor analysis (PARAFAC) has emerged, which enables identification of the primary modes of variability of fluorescence intensities and peak positions within an observational data set (Stedmon and Bro, 2008). PARAFAC has been previously applied to investigate DOM in drip waters by Rutledge *et al.* (2014, 2015) and as a measure for the amount of organics incorporated in calcite during lab experiments by Pearson *et al.* (2020).

Prior studies of fluorescence in groundwater and cave drip waters have indicated dominant peaks in humic-like components, with seasonally variable peak wavelengths (Baker and Genty, 1999). Compared to overlying soil-water fluorescence, spectra of drip water are likely to be blue-shifted (i.e., fluorescent peaks are shifted towards shorter wavelengths) because of the preferential adsorption of some humic-like DOM onto the bedrock (Jin and Zimmerman, 2010; Philibert *et al.*, 2022) and continued microbial degradation. Microbial (“protein-like”) fluorescence that is produced in the soil or karst (Xia *et al.*, 2022) or related to livestock above the cave (Mudarra *et al.*, 2011) also has been suggested to be present in cave waters (Birdwell and Engel, 2010). Yet, seasonal-scale drip water monitoring studies that relate fluorescence properties to drip water chemistry and active speleothems are lacking, whereas they appear to be crucial to better understand the processes leading to speleothem fluorescent layer formation.

In this study, we have analyzed the evolution of fluorescent DOM in drip water at multiple drip sites within La Vallina Cave, located in the northern Iberian Peninsula, to contribute to a better understanding of the spatial and temporal variations of organic matter in drip water and improve our understanding of stalagmite fluorescence signals. We characterized the components of drip water fluorescence using a PARAFAC model, and compared this model to vegetational gradients, climatic influences, cave conditions, and drip water chemistry ($\delta^{18}\text{O}$, $\delta^{13}\text{C}_{\text{DIC}}$, and selected trace elements; see Kost *et al.*, 2023). The analysis is extended through measurements of fluorescence in the dissolved bedrock and by CLSM images of actively growing stalagmites from the same cave. Using this combined data set, we evaluated the implications of using speleothem fluorescence for inferring past changes in landscape and climatic processes, and for the interpretation of annual to sub-annual fluorescence lamination in stalagmites.

STUDY SITE

Our study was conducted in La Vallina Cave on the northern part of the Iberian Peninsula, within the Cantabrian Mountains (43° 24.78'N, 4°48.22'W; Fig.1). The cave entrance is located 2.5 km from the coastline at an altitude of 70 m above sea level. La

Vallina formed within the Carboniferous dark sulfidic massive micritic limestone of the Barcaliente Formation. The bedding is sub vertical, dipping 70° to the North. The Barcaliente Formation is rich in amorphous organic matter and classified as containing types II and III kerogen (Álvarez et al., 2019). Numerous block falls throughout the cave are consistent with a seismically active shallow crust (Delavaud et al., 2012). Karstification has led to several dolines, recognizable topographically on the landscape above the cave.

In this study, we monitored organics in drip waters at seven locations in the cave (*FOR*, *GLO*, *GRA*, *MUS*, *PLA*, *SKY*, and *SNO*; shown in Fig. 1). Our sampling locations encompass a range of overlying land-cover conditions (Fig. 1), from dominantly forest (*FOR*, *SNO*) to shrubs with sparse interspersed trees (*GLO*, *GRA*, *MUS*) and pasture (*PLA*, *SKY*). Except for Mushroom (*MUS*), all sampling locations reside in the upper of two cave galleries. Additional details of the surrounding of each sampling location are listed in Table 1 and Supplementary Table 1. Currently, anthropogenic activities significantly influence the vegetation and the land area above the cave: parts of the land serve as pasture for farm animals, and the former primary deciduous forest, which was dominated by deciduous oak (*Quercus robur*), chestnut (*Castanea sativa*), and evergreen oak (*Quercus ilex*), has been partially exchanged with *Eucalyptus* trees that were introduced in the region in the nineteenth century for wood production. The densest tree cover is on the steeper hillslope near the entrance and the sampling location *FOR* (Fig. 1). The *Eucalyptus* tree ages are estimated to be around 60 years old, based on measurements of the stem diameter and empirical approximation by Ferrere et al. (2005). Additionally, based on the observed presence of charcoaled trees and regional agriculture history (Carrión et al., 2010; Carracedo et al., 2018), the parts of the land currently open or covered with fern (*Polypodiopsida*) likely were exposed to fire activity. Overall, these land-use changes, as well as the high water demand of *Eucalyptus* trees, are likely to have an effect on current water availability (Bosch and Hewlett, 1982; Ferreto et al., 2021), and thus cave hydrology.

Present-day regional climate, primarily controlled by proximity to the North Atlantic Ocean, is mild and warm. It can be classified as “Cfb” (temperate, with a warm summer but no dry season), according to the Köppen-Geiger classification (AEMET, 2011). The closest weather station (Llanes, 4.2 km NE of the cave, at the coast) has recorded precipitation of 1267 mm/yr and an annual mean temperature of 15.3°C for the study period May 2020–May 2021 (AEMET, 2021). The northern Iberian Peninsula is dominantly influenced by the westerlies. Most incoming precipitation originates from the Atlantic front systems and exhibits a long-term weighted annual mean $\delta^{18}\text{O}$ of -5.75 ± 0.34 ‰ (2000–2015 mean $\delta^{18}\text{O}$, Santander GNIP station, IAEA/WMO, 2022).

METHODS

Experimental methods

Drip water field campaign

Drip water samples were collected biweekly to monthly from May 2020 to May 2021 (the exact sampling dates were 20 May 2020, 28 May 2020, 24 June 2020, 7 August 2020, 11 September 2020, 2 October 2020, 16 October 2020, 30 October 2020, 13 November 2020, 11 December 2020, 16 January 2021, 13 February 2021, and 16 May 2021). In autumn, biweekly sampling was carried out to assess the effects of increased precipitation and falling leaves on drip water chemistry and fluorescence. Monitoring

took place over the entire year at four locations (*GRA*, *GLO*, *SKY*, *PLA*), from 11 September 2020 onwards at location *FOR*, and only for the last three dates at *MUS* and *SNO*. Individual drip water samples were collected directly into amber glass vials that previously had been combusted at 450°C for 4 hours and then were shipped to ETH Zürich.

The monthly sampling frequency is sufficient to identify seasonal-scale changes in drip water fluorescence, but it is worth noting that fast-changing fissure-flow dynamics could have been underestimated. However, with one exception (*FOR*), the sampled sites were classified at the boundary between seepage flow and seasonal drip based on the variation in drip rate, suggesting a dominant matrix-flow component with less influence from fissure flow (Kost et al., 2023). Long-term trends and interannual variability were not examined in this study because the entire time series was only one year long.

In a separate study (Kost et al., 2023), the conditions at the sampling site and the chemistry of splits of the same water samples were analyzed. In our discussion section, we make use of parts of the results from Kost et al. (2023) to directly compare drip water fluorescence to cave conditions at the drip site and drip water chemistry. Specifically, the recorded cave temperature and drip rates at sampling sites are employed here, as well as measurements of drip water $\delta^{18}\text{O}$, $\delta^{13}\text{C}_{\text{DIC}}$, and drip water concentrations of Sr, Cu, Y, and Ca. The drip water chemistry analysis methods are described in full detail in Kost et al. (2023). Drip water $\delta^{18}\text{O}$ variance and normalized drip rate for each site have been computed separately for this study using only data from the exact dates for which fluorescence and drip water measurement data are available (the compiled data set is given in the Supplementary section). The drip rate was normalized by dividing the value on the sampled date by the highest value obtained at this site over the whole monitoring period, as described by Kost et al., 2023.

Additional collection of bedrock, active speleothems, and site information

During the course of sample collection, additional data on the study site was acquired. Measurements of bedrock thickness above the cave sampling locations (Table 2) were carried out by combining a new precise topography of the cave interior and high-resolution exterior GPS measurements. The cave topography was generated using a calibrated Leica Disto X310 (Heeb, 2009, 2010) and Brunton ComPro0-360° compass. The exterior reference points above the cave were measured using high precision GPS (Hi-Target Inno) with GNSS receptor Hi-Target. Vegetation evolution and animal presence above the cave were noted regularly in the field report and incorporated in the present map (Fig. 1). Active speleothems close to the drip water sampling locations were collected on multiple occasions and are already described in detail in Sliwinski et al. (2023). The analyzed bedrock sample was collected close to the sampling location *SKY*.

Drip water absorbance and fluorescence measurements

Drip water samples were stored at 4°C in a refrigerator without other biological samples or organic solvents. Samples were measured between one month and one year after collection, and it was double-checked that storage time did not affect the results by re-measuring selected older samples (Supplementary Fig. 1). Due to turbidity in the source water, some particulate matter might be suspended in natural water samples, which is why natural water samples are commonly filtered before measuring fluorescence. However, tryptophan-like fluorescence in particular has

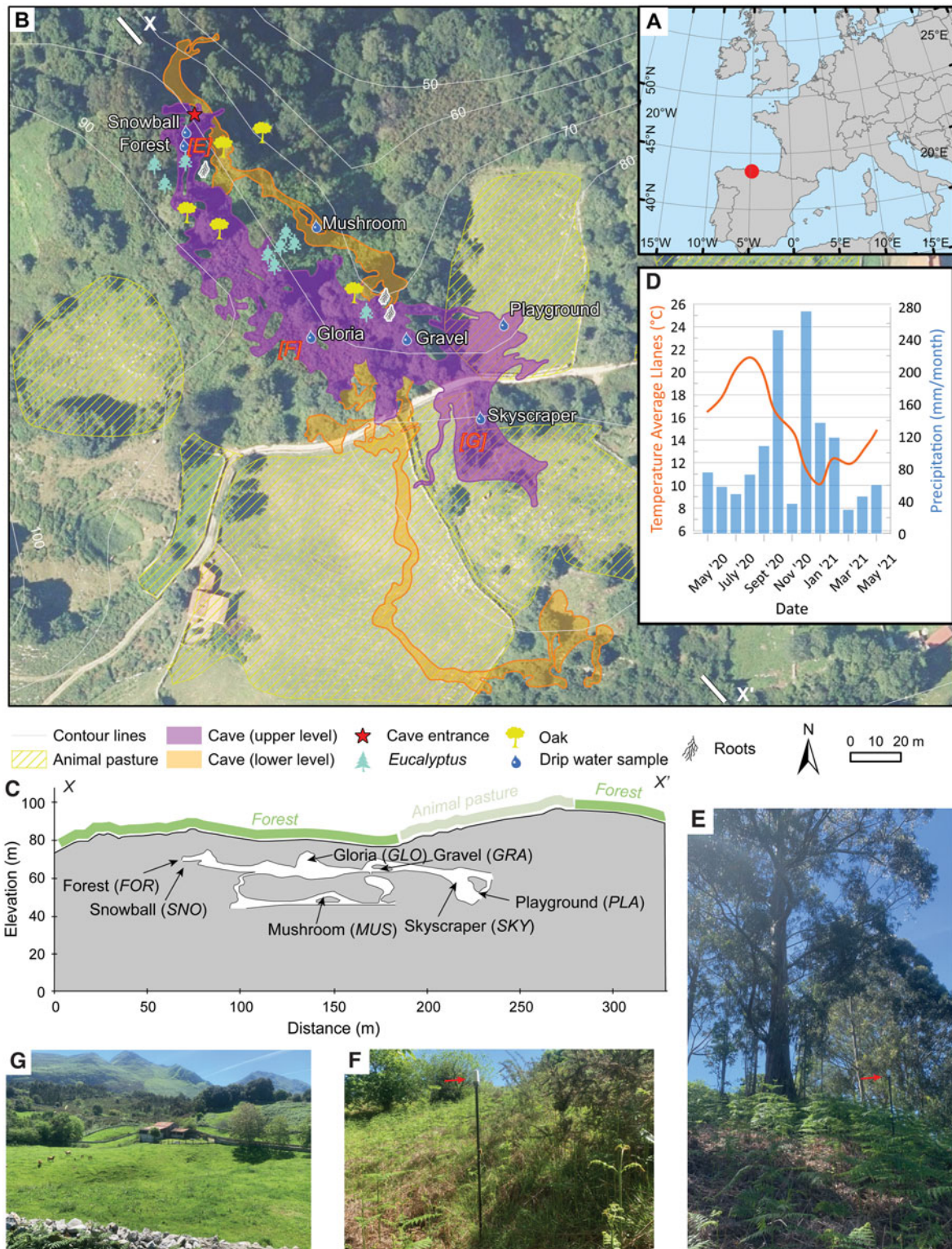


Figure 1. Studied area. (A) Reference map with red circle denoting the cave location. (B) Plan map of the cave upper gallery (green outline) and lower gallery (orange outline) indicating the location of drip water sampling (labeled drop symbols) overlaid on aerial image from 2017 (Plan Nacional Ortofotografía Aérea - PNOA of Spanish IGN; available at <https://centrodedescargas.cnig.es>; last access: 30 December 2022), and showing topographic contours (white lines) with elevation above sea level (m). Pasture use, large trees, and the position of root systems penetrating the cave are noted based on our own field observations. (C) Cross section (X–X') of the cave with projected sampling locations, based on our Leica Disto X310 survey. (D) Monthly mean air temperature and cumulative precipitation from Llanes weather station over the sampling period (AEMET, 2021). Llanes weather station is located directly at the coast, 4.2 km NE of the cave. (E) Image of vegetation above the cave entrance, dominated by *Eucalyptus* trees. The red arrow marks the position of the GPS, which here is placed at the position of a prominent root feature seen in the cave, close to the entrance and sampling locations FOR and SNO. (F) Image of intermediate, fern-dominated vegetation. The red arrow marks the position of the GPS above the sampling location GLO. (G) Image taken above sampling location SKY (towards SW), highlighting the extent of agriculture in the doline-shaped landscape.

Table 1. Sampling locations discussed in this study, their overall cave properties, and mean optical values. Variability is given in the form of one standard deviation (1SD). Overall fluorescence over the entire EEM is given in Raman units (R.U.). FI is the fluorescence index (McKnight et al., 2001). In the first column, the dominant vegetation type forested, intermediate cover (intermed.), and pasture are given, but extended descriptions of the overlying vegetation and cave setting can be found in Supplementary Table 1. Cave temperature, pCO₂, and cover thickness have been reported previously in Kost et. al (2023). The drip rates and the δ¹⁸O variance were recalculated based on measurements from the same study but only for the time period covered in this fluorescence study.

Location	Cave Temp.(°C)	pCO ₂ (ppm)	Cover thickness (m)	Drip rate (ml/min)	δ ¹⁸ O	Overall fluorescence (R.U.)	FI	Spectral slope	C3:(C1+C5) ratio
(Abbr.) Veg. type	monthly mean	Max		Mean	variance	Mean	Mean	Mean	Mean
	(1SD)	(Min)		(1SD)		(1SD)	(1SD)	(1SD)	(1SD)
Forest (FOR) forested	14.21 (0.56)	1496 (461)	14.5	0.35 (0.18)	0.477	47.4 (13.35)	1.66 (0.02)	1.14 (0.3)	0.25 (0.17)
Snowball (SNO) forested	14.21 (0.56)	1496 (461)	14.4	—	—	37.86 (12.15)	1.60 (0.03)	0.62 (0.21)	0.18 (0.14)
Gloria (GLO) intermed.	14.44 (0.27)	1582 (569)	8.7	0.22 (0.08)	0.09	22.56 (24.64)	1.65 (0.12)	0.99	0.76 (0.7)
Gravel (GRA) intermed.	13.9 (0.22)	2416 (509)	13.3	0.72 (0.38)	0.08	18.64 (19.32)	1.52 (0.16)	1.15	0.37 (0.25)
Mushroom (MUS) intermed.	13.6	—	23.2	—	—	10.87 (0.23)	1.55 (0.2)	0.91	0.22 (0.46)
Skyscraper (SKY) pasture	13.89 (0.17)	5390 (510)	27.6	89.22 (24.25)	0.05	26.76 (20.35)	1.72 (0.16)	0.83	0.47 (0.50)
Playground (PLA) Pasture	13.72 (0.16)	4199 (525)	29.5	1.22 (0.916)	0.04	20.34 (5.73)	1.73 (0.14)	−0.48	0.96 (0.57)

been shown to decrease significantly through the filtering process (Baker et al., 2007). Because the expected turbidity of our samples was low due to the primarily laminar flow through the karst, we did not apply any filter processes.

Drip water absorbance spectra and fluorescence excitation-emission matrices (EEM) were measured simultaneously with a Horiba AquaLog spectrofluorometer using 4 seconds integration time and an excitation wavelength step of 3 nm or 5 nm. Quartz cuvettes with a path length of 1 × 1 cm were rinsed several times with nanopure water before and after each measurement. During post-processing, EEMs with 3 nm resolution were converted to the coarser 5 nm resolution by bicubic interpolation to enable parallel factor (PARAFAC) analysis and increase comparability between individual measurement days. EEMs were exported from the R1/C1 AquaLog output with respective excitation and emission wavelengths of 240–600 nm and 240–800 nm. Further post-processing, performed with eemR (Massicotte, 2019), included blank subtraction, inner-filter effect correction, Raman/Rayleigh scatter removal, and Raman normalization. EEM visualization uses the scientific color maps *batlow* (Cramer et al., 2020). Intensities are given in normalized Raman units (R. U.), and data variability is expressed as one standard deviation.

Dissolved bedrock fluorescence measurements

The possible contribution of bedrock to total drip water fluorescence was investigated by dissolving three 2-mg aliquots of drilled powder samples in 4.5 ml of 0.025 M HCl (analogous to Pearson et al., 2020). The aqueous solution was brought to a pH of 5–7 by titration with NaOH. Dissolved bedrock absorbance spectra and

fluorescence EEM were post-processed identically to drip water and were measured on the same instrument with an integration time of 10 seconds and a step size of 5 nm.

Confocal laser scanning microscopy (CLSM) of speleothems and bedrock

Solid-phase fluorescence in three active stalagmites and one bedrock sample was investigated with CLSM. Measurements were performed at the Scientific Center for Optical and Electron Microscopy of ETH Zurich using an Olympus Fluoview 3000 and the methodology of Sliwinski and Stoll (2021). An excitation wavelength of 488 nm and a 490–590 nm detection window were used, resulting in an optical slice thickness of < 10 μm with a 10 × objective. In contrast to the scan across a wavelength range carried out for the drip water EEMs, the excitation wavelength was fixed at one wavelength for the CLSM images. Consequently, the nature of the fluorophores cannot be characterized in more detail from the images. Retrieved images were mirrored to represent the original orientation, and a scale bar was added using Fiji (Schindelin et al., 2012).

Data analysis methods

Fluorescence index

A typical measure for describing fluorescent DOM and contrasting it with other water samples of various origins and DOC concentrations is the fluorescence index (FI) (McKnight et al., 2001). The FI is computed as the ratio of emission intensity at 470–520 nm at a fixed excitation wavelength of 370 nm for instrument-corrected spectra. Low values of FI (~1.2) indicate

Table 2. Properties of the derived 5-component parallel factor analysis (PARAFAC) model. Ex_{max} and Em_{max} give wavelengths of peak excitation-emission pairs (double peaks for humic-like components). Pearson correlations between individual components across all samples are given in the column Fmax correlation in the top right triad. The bottom left triad indicates the respective p -values (italic, in brackets). Components are described by comparison to literature^(1–6) and the OpenFluor^(7–9) database (¹Coble et al., 2014; ²Aitken et al., 2014; ³Xia et al., 2022; ⁴Zhou et al., 2013; ⁵Yamashita and Jaffé, 2008; ⁶Cory and McKnight, 2005; ⁷Chen et al., 2018; ⁸Dandrilli and McConnell, 2021; ⁹Wünsch et al., 2015).

Component	Ex_{max} (nm)	Em_{max} (nm)	Description (from literature and OpenFluor)	Fmax correlation				
				C1	C2	C3	C4	C5
C1	240; 320	408	humic-like C ¹ , higher molecular weight vegetation ¹	1.00	0.04	0.50	−0.12	0.62
C2	265	291	amino acid-like ¹ , tyrosine ¹ , simple tannin ^{2,8} , found in cold waters ⁷	(0.72)	1.00	0.5	0.5	0.08
C3	240; 280	333	humic-like M ¹ , marine planktonic ¹ , microbially processed ^{1,3} , oil ⁴ , indigenous organics from bedrock (this study)	(<0.01)	(<0.01)	1.00	−0.02	0.28
C4	255	277	amino acid-like ¹ , close spectral match to phenylalanine ⁹	(0.36)	(<0.01)	(0.89)	1.00	−0.10
C5	256; 370	455	humic-like ¹ , Soil fulvic acid ⁵ , terrestrial higher plants ⁶	(<0.01)	(0.51)	(0.03)	(0.43)	1.00

more terrestrial input, whereas higher values (~1.8) point towards more microbial sources (Gabor et al., 2014).

PARAFAC modeling

PARAFAC analysis (Stedmon and Bro, 2008) was used to investigate DOM fluorescence variability in the spatial and temporal domains. Over the last decade, PARAFAC modeling has become a standard approach for EEM interpretation due to the possibility of recognizing site-specific peaks instead of referring to general literature (Coble et al., 2014). In this study, a global five-component model was computed from 65 corrected EEMs by staRdom (Pucher et al., 2019) with non-negative constraints, a model tolerance of $1e^{-8}$, 40 models, and 10,000 maximum iterations. All models converged with these settings, and no additional outliers were found. Validation with a regular split-half analysis was not considered statistically robust due to the high variability between the sites and the small sample size of < 100 (Pucher et al., 2019). Instead, separate local PARAFAC models of the five main sampling sites were computed using only three components. To compare local models to the global five-component model, shape-sensitive congruencies (SSC) (Wünsch et al., 2015) were computed for each combination to quantify similarities between the individual components in the two models (Supplementary Fig. 2), which showed that the five-component global model represented the individual sites well. Because the spectral peaks cannot be clearly linked to specific substances, care must be used when interpreting EEM observations and PARAFAC models. Additionally, PARAFAC modeling may create artifacts instead of biologically relevant signals, and changing experiment conditions (e.g., pH or temperature of drip waters) can influence the peak intensities and positions (Aiken, 2014). Nevertheless, as demonstrated by numerous applications, PARAFAC modeling can be used successfully to describe properties of drip water fluorescence in more detail, with a comparably rapid measurement method.

The final PARAFAC model was uploaded to the OpenFluor database (Murphy et al., 2014) to compare peaks with published PARAFAC models. Model stability, which was assessed with the core consistency diagnostics CORCONDIA (Bro and Kiers, 2003), was 79.65%. PARAFAC components were visualized using the scientific color map *ajolla* (Crameri et al., 2020).

Calculation of absorption spectra and slope ratio

In addition to the fluorescent measurements, the optical properties of DOM can be characterized by simultaneous absorption measurements with the AquaLog spectrofluorometer. The fraction of total DOM that absorbs UV and visible light is termed chromophoric dissolved organic matter (CDOM). CDOM can overlap with the fraction of fluorescent dissolved organic matter (FDOM), but it is not necessarily the same. Here, we analyzed absorbance separately for additional information about the origin and composition of the samples. To this purpose, absorbance measured with Aqualog was converted to the absorption coefficient α following Beer's law (Supplementary Equation 1). We used the absorption α as a quality check to test whether the unfiltered samples are optically dilute enough. Values for α were well below 0.1 for all samples and measured wavelengths except for GRA on 7 August 2020, which showed evidence of mud contamination already during collection and subsequently was considered an outlier. Two samples containing negative absorbance values were also disregarded for absorbance analysis.

To compare the absorption spectra to other studies, a slope ratio between a shorter (275–295 nm) over a longer (350–400 nm) wavelength region was computed analogously to Helms et al. (2008). The two slopes, $S_{275-295}$ and $S_{350-400}$, were calculated by fitting a linear model through the natural logarithm of the absorption spectra values in the respective wavelength regions. By convention, positive slope values are given for a decrease with higher wavelengths to fit the expected exponential decay.

RESULTS

Fluorescence characteristics

Drip water fluorescence and PARAFAC model

Fluorescence in the drip water was detected at all sampling sites (mean fluorescent properties are presented in Table 1). The overall mean fluorescence over the entire EEM region ranges from 10.88 ± 0.23 R.U. (*MUS*) to 47.40 ± 13.34 R.U. (*FOR*). The FI ranges from 1.52 ± 0.16 (*GRA*) to 1.73 ± 0.14 (*PLA*).

The principal peaks and modes of variability in fluorescence across all collected drip water samples are identified with PARAFAC analysis. We present a five-component model, which explains 88% of the total variance within the entire data set

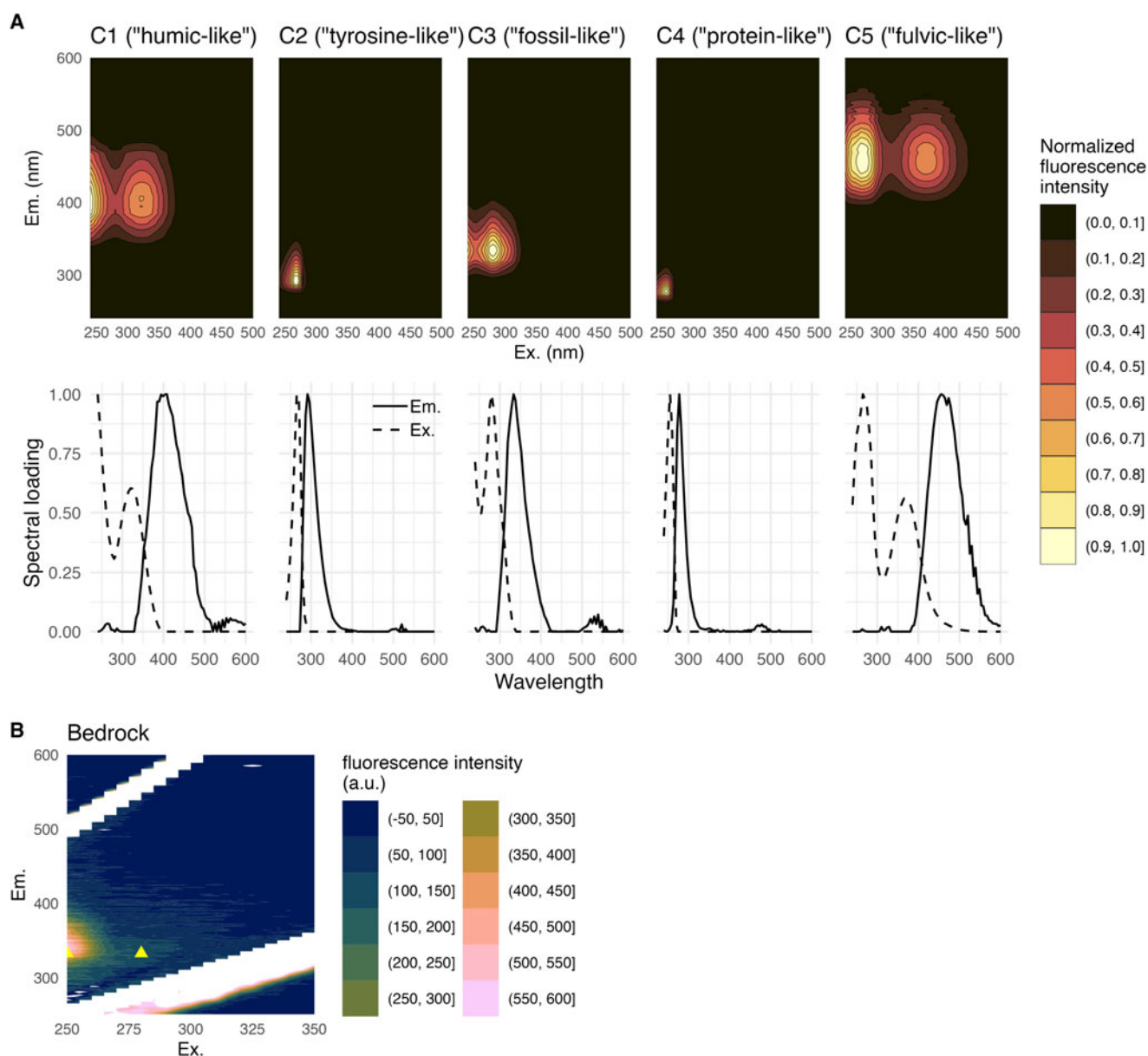


Figure 2. Drip water parallel factor analysis (PARAFAC) model and bedrock endmember excitation-emission matrix (EEM). **(A)** Drip water 5-component PARAFAC model and its spectral loadings. Fluorescence intensity is normalized to unity. Spectral loadings maxima in emission and excitation wavelengths are indicated with solid and dashed lines, respectively. **(B)** EEM of dissolved organic-rich bedrock. Fluorescence intensity is given in arbitrary units (a.u.). Yellow triangles indicate peak positions of drip water PARAFAC component C3 for comparison.

(Fig. 2A and Table 2) and serves as a base template for further interpretation of the individual locations. The components, named C1 to C5, are normalized to unit intensity and are ordered by the fraction of variance explained. The dominant feature of the odd PARAFAC components (C1, C3, C5) is the occurrence of a double peak within the EEM (Fig. 2A). C1 shows two excitation peaks (Ex_{max}) at 240 nm and 320 nm, respectively, and an emission maximum (Em_{max}) at 405 nm. The components C3 ($Ex_{max}/Em_{max} = 240/305$ nm and $Ex_{max}/Em_{max} = 280/305$ nm), and C5 ($Ex_{max}/Em_{max} = 265/455$ nm and $Ex_{max}/Em_{max} = 370/455$ nm) mark spectra that are blue- and red-shifted compared to C1, respectively. In contrast, the two even components (C2, C4) contain single peaks with low Ex/Em wavelengths and narrow spectra (C2 $Ex_{max}/Em_{max} = 265/291$ nm; C4 $Ex_{max}/Em_{max} = 255/277$ nm).

Bedrock fluorescence

We dissolved the organic-rich bedrock to investigate a possible contribution to overall fluorescence from indigenous fluorescence due to bedrock leaching. The resulting EEM (Fig. 2B) features a double peak structure centered around $Ex/Em = 245/337$ nm and $Ex/Em = 280/337$ nm. A comparison of the bedrock-derived EEM (Fig. 2B) with the PARAFAC model yields a strong similarity to component C3 (Fig. 2B, yellow triangles).

Confocal laser scanning microscopy (CLSM) of active speleothems and bedrock

Our CLSM images (Fig. 3A–C) reveal some sectors in the actively growing stalagmite from beneath the SKY and SNO drip locations with fine-scale lamination, which may be annual to subannual

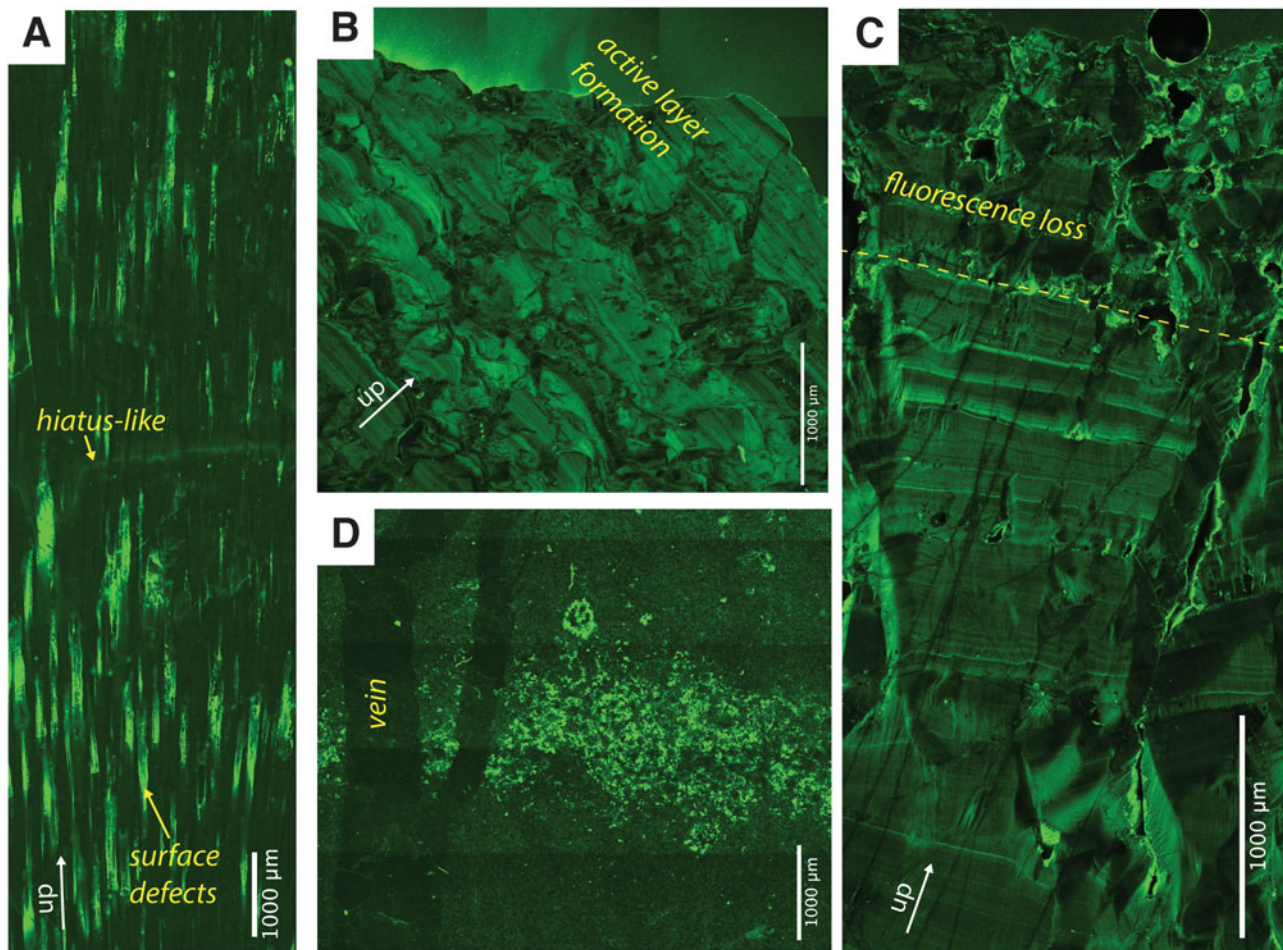


Figure 3. Solid-phase fluorescence features of actively growing speleothems and bedrock from La Vallina Cave. (A) Stalagmite PG-2, sampled 5 m from drip water point *PLA*; (B) stalagmite *SKY*, sampled beneath the drip water sample point *SKY*; (C) stalagmite *SNO*, sampled beneath the drip water sample point *SNO*; (D) polished bedrock. CLSM images were created with an Olympus Fluoview 3000 generated by excitation at 488 nm and detection at 490–590 nm; images were post-processed with Fiji (Schindelin et al., 2012) and Adobe Illustrator. Bomb spike age models for these active stalagmites are presented in Sliwinski et al. (2022).

according to available age models from ^{14}C (Sliwinski et al., 2023). These rapidly growing stalagmites feature high porosity and many crystal defects, which contribute to lateral discontinuity in fluorescent lamination, as described in previous studies (Sliwinski and Stoll, 2021; Sliwinski et al., 2023). The polished bedrock sample, dominated by a C3-like component in dissolved form, also indicates pronounced fluorescence, which appears to be concentrated in certain sectors of the image.

Spatial and temporal variability of drip water absorbance and fluorescence

Drip water optical properties (summarized in Table 1) vary substantially among sampling locations. The absorption coefficients of UV and visible light show the typical exponential decrease with increasing wavelength across sampling locations (Fig. 4A). In *PLA* and *GLO* the median absorption spectra show secondary intensity peaks around 295 nm and 350 nm, respectively. *PLA* consequently has a significantly different slope ratio ($p < 0.05$, Tukey-test), because the spectral slope $S_{275-295}$ is negative for *PLA* due to the secondary peak (Fig. 4B). Although a negative $S_{275-295}$ value is a deviation from the expected exponential decay, similar features

previously have been found in cave spring waters (Birdwell and Engel, 2010).

Plotted by sampling location, the average and standard deviation fluorescence EEM plots show substantial variations in peak distribution (Fig. 5). Sampling locations *FOR* and *SNO*, in which oak and *Eucalyptus* trees dominate, exhibit both similar average patterns and variability, with a dominant relative contribution from the components C1 and C5 (Fig. 5A, B). In contrast, C2, C3, and C4 intensities are rather low. *GLO* and *GRA*, located in shallow depths and covered by ferns and solitary trees, exhibit comparable total fluorescence, but much greater contribution of C2 and C4. The lowest total fluorescence and most constrained variability are found in *PLA*, which is covered by pasture, and *MUS*, which is covered by ferns and singular trees. Despite similar land cover at *PLA* and *SKY*, *SKY* features higher overall fluorescence.

Over the year, the PARAFAC model components C1 and C5 feature more constant concentration on a drip site-specific intensity level without strong seasonality (Fig. 6). In contrast, C2 and C4 intensities consist of short-lived peaks and vary substantially on the seasonal timescale in most monitored locations, especially in *GLO* and *GRA*. C3 appears more constant in some locations, but variable in other sites. Abrupt decreases of fluorescence

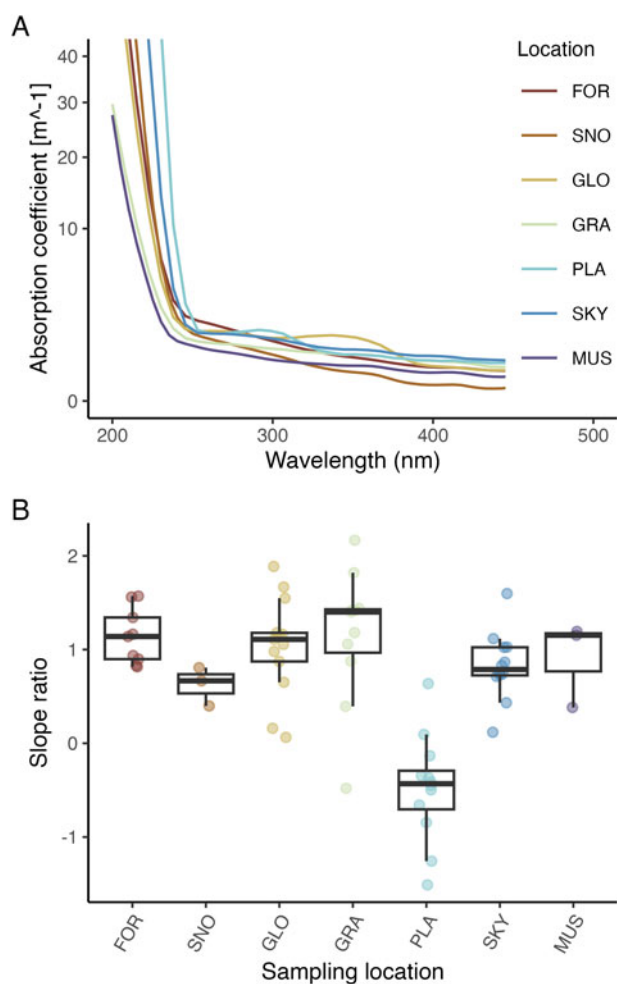


Figure 4. Absorption properties of drip water samples for each sampling location. (A) Loess smoothed median absorption spectra for all locations. (B) Spectral slope ratio values for individual absorbance measurements.

intensity in components C2 and C4 (e.g., in October 2020) occur mainly concurrently across sampling sites. In contrast, C3 intensity peaks do not occur simultaneously across drip sites. For example, increased values in *FOR* in autumn are contrasted by especially low C3 values in *SKY*.

DISCUSSION

Significance of absorbance and attribution of PARAFAC components to sources of DOM

Several features of the measured absorbance are environmentally relevant. The observed decrease of the absorption coefficient in drip waters (Fig. 4A) is steep compared to samples from surface or swamp waters (e.g., Helms et al., 2008), likely due to the higher amount of filtering occurring in the carbonate aquifer. The secondary absorption peaks around 295 nm and 350 nm in *PLA* and *GLO*, respectively, theoretically could occur due to spectral interferences with larger colloids, but the overall absorption coefficients of our samples are $< 0.1/\text{m}$. Absorption coefficients in this bandwidth also could be altered by compounds such as tryptophan or uric acid, which show local deviations in this wavelength region when measured in isolation (Spangenberg et al., 2021). *PLA* is located below pasture and a doline; the presence of uric

acid, originating from cattle, seems plausible but would need to be confirmed by future analysis of compounds by liquid chromatography-mass spectrometry.

Drip water DOM can be characterized by comparing the dominant peaks of the fluorescence data set found by the PARAFAC model to literature and the OpenFluor database (Murphy et al., 2014). In our model (Fig. 2A, Table 2), the dominant feature of odd PARAFAC components (C1, C3, C5) is the occurrence of a double peak within the presented EEM. This slightly blurred double-peak structure is characteristic of aquatic humic substances, most likely because families of humic compounds share a common fluorophore backbone but have different ring substitutions, leading to multiple Ex/Em maxima (Coble et al., 2014). Component C1 can be explained as Peaks A_c and C of the Coble nomenclature, also called Humic C (Coble et al., 2014). This kind of fluorescence is commonly attributed to humic-like components with high molecular weight and aromatic organic compounds derived from plant litter (Coble et al., 2014; Stedmon and Cory, 2014). In La Vallina drip waters, C1 is interpreted to originate mainly from the vegetation above the cave and includes compounds derived from plant litter, such as lignin. Component C5, which is shifted towards longer peak wavelengths than C1, has been attributed to soil fulvic acid (Yamashita and Jaffé, 2008) and higher terrestrial plants (Cory and McKnight, 2005). Compared to C1, C5 is interpreted to contain terrestrial material that is less degraded by photobleaching or microbial activity, such as remainders of leaves. Yet, the C5 emission peak wavelength from our model (Ex/Em = 256/455 nm and Ex/Em = 370/455 nm) is slightly lower than expected for this peak in the literature (Ex/Em = 250/470–504 nm and Ex/Em = 320–365/470–504 nm), coined as Humic C+ (Coble et al., 2014). Our C5 peak might contain some Humic C+, but overall, because it is much weaker than expected (based on studies investigating active carbon adsorption [Philibert et al., 2022]), we hypothesize that a significant fraction of the Humic C+ component has been preferentially adsorbed on the bedrock and is subsequently absent in the drip water PARAFAC model presented here. Component C3, shifted towards shorter peak wavelengths, aligns well with the peak Humic M (Coble et al., 2014). Peak M, which has been detected primarily in marine planktonic environments, has been attributed to new biologically produced fluorescent material and degradation processes such as breaking bonds in Humic C fluorophores (Coble et al., 2014). Such fluorophores have also been found in fresh waters (Stedmon et al., 2003) and recently have been shown to be produced within the lower soil or epikarst by planktonic, heterotrophic bacteria feeding from plant litter (Xia et al., 2022). In addition, C3 matches the EEM of fossil-like (degraded oil) compounds derived from ancient marine organic matter (Zhou et al., 2013). In our study, component C3 further closely matches the spectral peaks of dissolved bedrock EEM. We, therefore, propose that material leached from the ancient marine and organic-rich bedrock is a significant additional source for C3 fluorescence in this study, especially for drip sites featuring longer residence times. To our knowledge, such a contribution of fossil organic matter to drip water fluorescence has not been considered previously in the literature.

The two even components, C2 and C4, contain single peaks with low Ex/Em wavelength pairs and narrow spectra in the presented EEM. Such peaks previously have been attributed to organic compounds with a lower degree of conjugation, especially microbial amino acids (Coble et al., 2014) and metabolism (Elliott et al., 2006), but also plant-derived simple phenols,

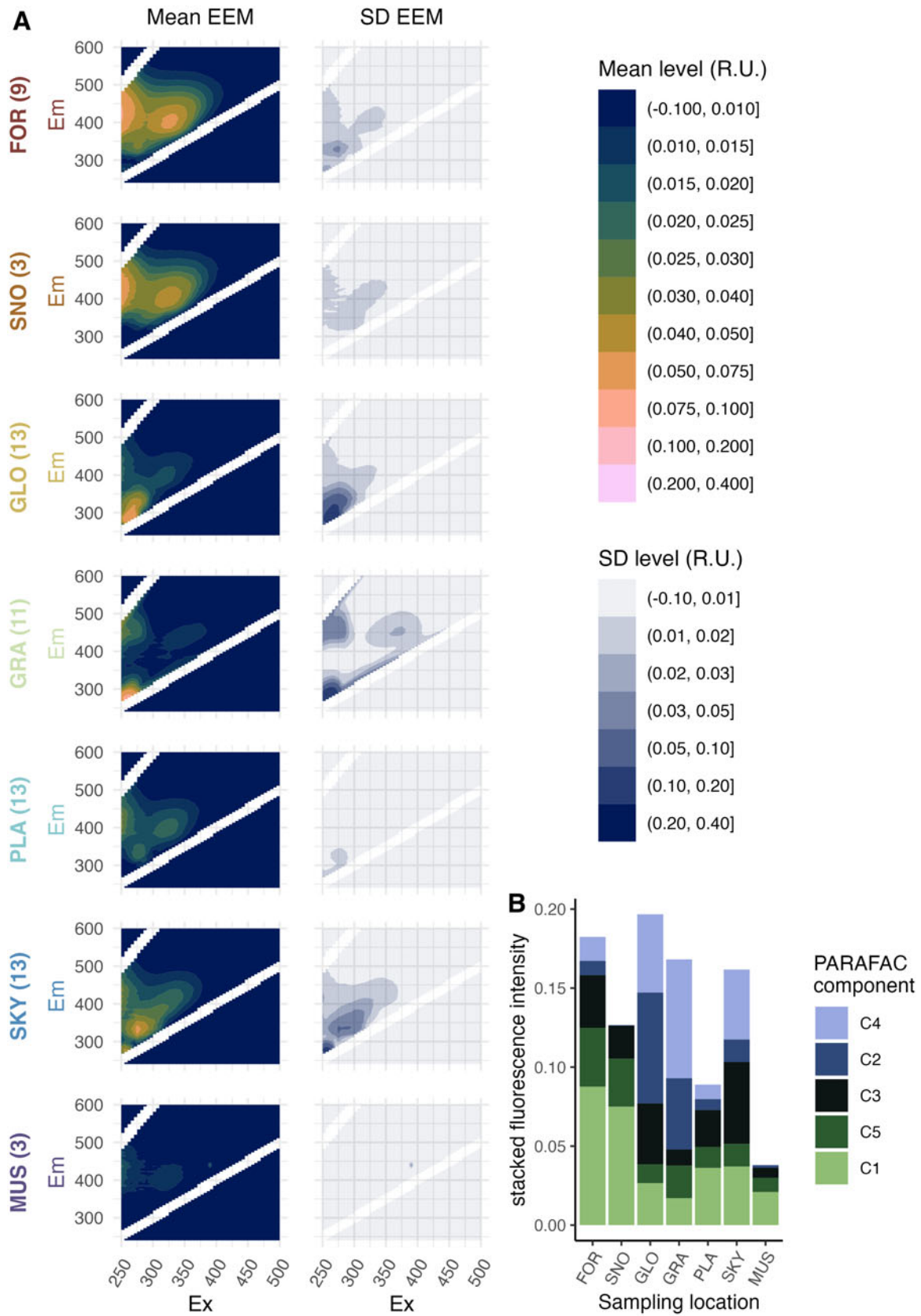


Figure 5. Spatial distribution of fluorescence across drip sites. **(A)** Mean and standard deviation (SD) of excitation-emission matrices (EEM) for each sampling location compiled over the monitoring period. Fluorescent intensities are given in Raman units (R.U.). **(B)** Mean intensity of all PARAFAC components for each sampling location, stacked to illustrate the total PARAFAC characterized fluorescence intensity at each location. C1 and C5 are described as “humic-like” and “fulvic-like,” respectively. C3 is described as “fossil-like,” C2 is described as “tyrosine-like,” and C4 is described as “protein-like.”

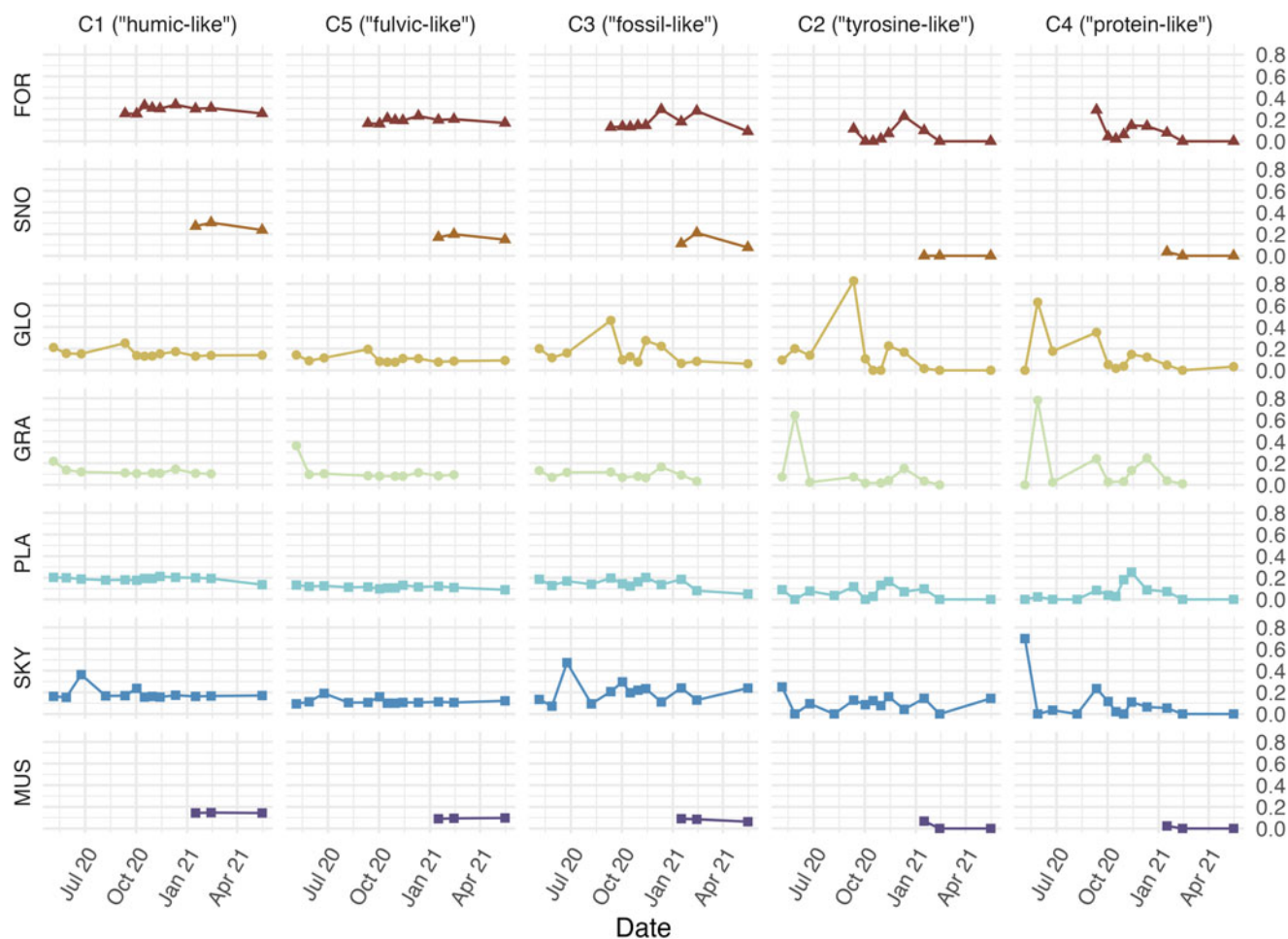


Figure 6. Temporal evolution of the 5 components of the PARAFAC model throughout the monitored period at each site. Each component y axis is given in normalized PARAFAC fluorescence intensity.

indoles, and tannins (Aiken, 2014). Compared to the OpenFluor database, spectra similar (similarity scores in Ex and Em > 0.95) to C2 of our model have been reported from Arctic waters and have been described as tyrosine-like (Chen et al., 2018). A similar peak structure also has been found in EEMs from melted ice cores, characterized as a tannin-like or more processed microbial signal (Dandrilli and McConnell, 2021). While some tannin might be present from the *Eucalyptus* trees in La Vallina drip waters, we find microbial activity the more likely source because the observed seasonal variability of C2 is similar to C3 and C4, which are also interpreted to be microbially altered. Additionally, the C4 spectrum is similar to the amino acid phenylalanine, measured as a single compound (Wünsch et al., 2015). Because phenylalanine is a relatively hydrophobic amino acid (Öncel et al., 2005), we propose that C4 might reflect a local signal originating from the lower soil or epikarst.

Overall, the analysis of absorbance and the PARAFAC model reveal several distinct sources of fluorescent and absorbent DOM (Fig. 7). Yet, the results also point towards a rather complex interaction among soil, karst, and drip water fluorescence, which are likely to be reflected in the speleothem fluorescence. Future studies could provide more specific information on the compounds present and their origin by employing electrospray ionization Fourier transform ion cyclotron resonance mass

spectrometry (ESI-FT-ICR-MS) (Lechleitner et al., 2017) or Liquid Chromatography Organic Carbon Detection on drip waters.

Relationship of fluorescence to cave settings

Humic-like fluorescence is generally expected to decrease with longer transport and karst residence time because the organic matter can be degraded by microbial activity (Fairchild and Baker, 2012) and especially humic-like compounds are likely to adsorb on the bedrock (Jin and Zimmerman, 2010; Philibert et al., 2022). Within our data set, depth is not a dominant control on humic-like fluorescence (Fig. 8A). Highest values are found in FOR and SNO, which are covered by forest, with a cover thickness of 14.35–14.47 m. The strong humic-like fingerprint is consistent with a higher amount of plant litter and soil products, initiated by the trees and expected to be transported to the respective drip sites. In contrast, humic-like fluorescence is lower in the shallow locations GLO and GRA and no decrease can be found compared to the deepest locations PLA and SKY. Yet, for sites of comparable land cover (GLO, GRA, MUS), the deepest site (MUS) does feature lower total fluorescence, which could be due to greater degradation or loss in transit to the deeper site. However, these three sites feature similar total C1+C5 fluorescence; therefore, it is also possible that instead of a depth-driven process, the additional

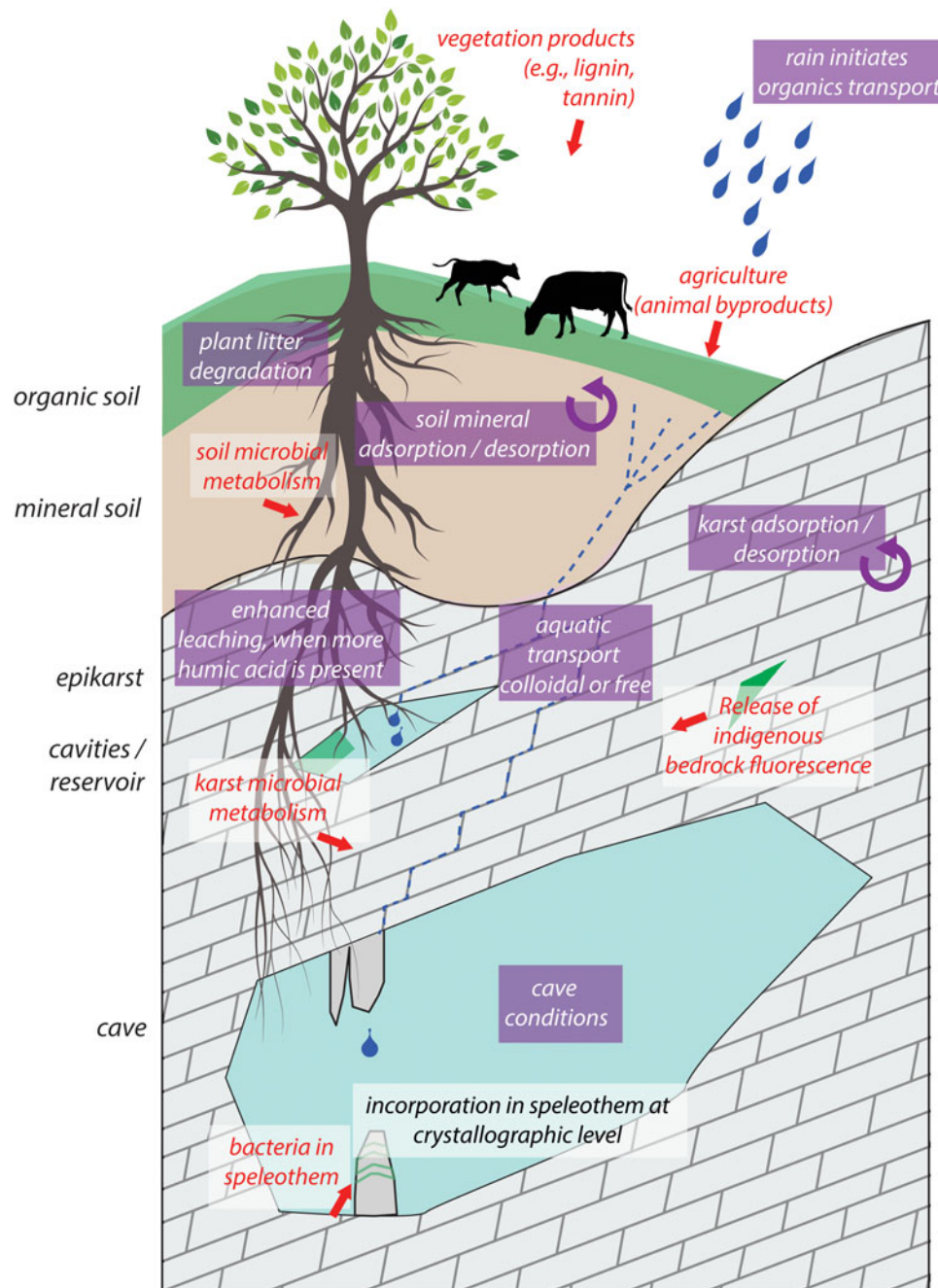


Figure 7. Schematic diagram of processes contributing to the observed drip water fluorescence, from vegetation through soil, epikarst, and into the cave. Red labels denote potential end-member sources of different fluorescent organic component classes. Lavender boxes highlight proposed interactions among climate, vegetation/plant litter, and bedrock including dissolution or leaching of bedrock by respired CO₂, and adsorption of fluorescent matter to bedrock, as well as cave conditions potentially affecting incorporation of fluorescent organic matter in speleothems.

livestock activity at *GLO* and *GRA* may contribute to the additional C2, C3, and C4 intensity relative to *MUS*.

In this setting, the variance of drip water $\delta^{18}\text{O}$ may be a useful indicator of drip water residence time (Kost et al., 2023). This is because individual rain events feature considerable $\delta^{18}\text{O}$ variability (Stoll et al., 2015; Moreno et al., 2021), but mixing within the karst reservoir leads to dampening of this signal to varying degrees at different drip sites. The greatest dampening of event scale variation (i.e., those with the lowest variance in drip water $\delta^{18}\text{O}$) are inferred to be characterized by the longest

residence times and greatest mixing of infiltration events. Here, the $\delta^{18}\text{O}$ variance is calculated from the data in Kost et al. (2023) only for drip water sites monitored for at least nine samplings over nine months. $\delta^{18}\text{O}$ variance is notably much greater for the location *FOR* than for the other calculated sites (*PLA*, *SKY*, *GLO*, *GRA*), indicating a shorter residence time. Similarly, *FOR* features higher total C1+C5 fluorescence, indicative of a high proportion of non-processed, humic compounds of vegetable origin compared to other sites with longer residence times (Fig. 8B).

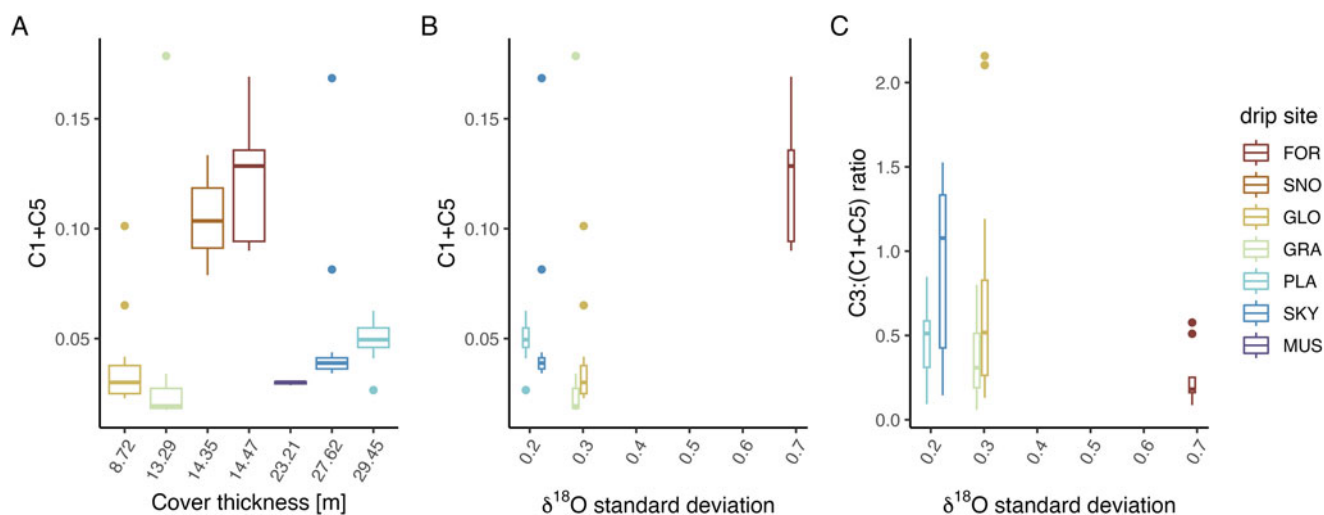


Figure 8. Overview of the relationship between fluorescence and cave settings. (A) Comparison of the summed C1 and C5 (humic-like and fulvic-like) components plotted versus ascending thickness of bedrock cover over the drip water sampling site. (B) Comparison of summed C1 and C5 components plotted versus the drip water $\delta^{18}\text{O}$ variance. (C) Comparison of the ratio of C3/(C1+C5), interpreted as the ratio of reworked or fossil components to humic-like and fulvic-like components, plotted against the drip water $\delta^{18}\text{O}$ variance. The $\delta^{18}\text{O}$ variance is computed from data in Kost et al. (2023) and is thought to increase for shorter drip water residence times.

We calculated the ratio $\text{C3}/(\text{C5}+\text{C1})$ to assess the relative significance of reworked or fossil DOM relative to surface-vegetation humic- and fulvic-like inputs. This ratio correlates strongly with the humification index, which also has been used previously to estimate the ages of organic matter (Ohno, 2002). The $\text{C3}/(\text{C5}+\text{C1})$ ratio is lowest for the *FOR* site of shortest reservoir time, consistent with least microbial consumption and/or more bedrock adsorption of high molecular weight components (Fig. 8C). These trends are consistent with observations elsewhere that longer residence times lead to increased DOM processing through microbial transformation and adsorption reactions (Blyth et al., 2016; Lechleitner et al., 2017).

Additionally, water flux may influence the fraction of input fluorescence that arrives at the cave drip site. Although at similar depth and reservoir mixing inferred from $\delta^{18}\text{O}$ variance, the much lower drip rate of *PLA* (1.22 ± 0.916 ml/min, see Table 1) than *SKY* (89.22 ± 24.25 ml/min) correlates with a much lower average total fluorescence intensity (Fig. 5B). We hypothesize that the very high flux at *SKY* may saturate the absorbance capacity of the karst host rock, a mechanism described in Jin and Zimmermann (2010). In this framework, a lower drip rate and flux at *PLA* may result in a higher fraction of dissolved fluorescence components adsorbed by karst host rock, and resulting lower concentrations emerging in cave drip water.

The PARAFAC results point to the possibility of multiple land surface sources for the fluorescence components, including contributions from potential livestock and humic and fulvic vegetation signals (Fig. 7). These sources also could be modified further during transport through the karst system by microbial reworking and adsorption on the karst host rock. In conjunction with the previously reported spatial trends in total fluorescence and its composition, our analysis suggests that at comparable bedrock depth, higher density of trees and shorter water residence times favor higher relative contribution of fluorescence from humic-like sources of vegetable origin. Fluorescence components more likely of microbial origin dominate at sites with longer water residence times. For sites of comparable land cover and residence times, higher drip water flux (drip rate) correlates with a higher

total fluorescence, which might be related to bedrock absorption capacity.

Seasonal variations and relationship of fluorescence to rainfall and temperature

Relevant for further meaningful interpretation of the fluorescence signal within speleothems is also the dependence of drip water fluorescence on climatological parameters such as temperature and precipitation. We investigated this hypothesis by comparing the fluorescence dataset to climatological data from the nearby weather station Llanes (4.2 km NE of the cave, at the coast). Two equally sized groups of dry and wet conditions are compared for each location based on total rainfall amount in the 10 days prior to sampling (Fig. 9, top row). The analysis suggests that humic-like and fulvic-like components (C1, C5) are higher during wet conditions only for the location *FOR*, whereas all other locations show no change between the wet versus dry conditions, and *PLA* shows lower C5 for wet conditions. For C3, *FOR* shows higher values in wet conditions, whereas other sites (*PLA*, *SKY*) show either increased values for dry conditions or no difference (*GRA*, *GLO*). This contrasting behavior at *FOR* may reflect an aged soil or active microbial source of C3 at this site and its rapid transmission due to the low reservoir time of *FOR* drip water, versus deeper sites where C3 may be more significantly sourced from fossil bedrock OM and therefore decoupled from the precipitation regime. Yet, despite the short residence time in *FOR* and significant short-term variation of some trace elements reported by Kost et al. (2023), the variability of C1, C3, and C5 is relatively smooth and humic-like fluorescence remains present over the entire year. This constancy might be related in part to water residence times, but it may also or additionally reflect a buffering of the concentration of humic components by sorption processes in the karst reservoir. Abiotically, humic-like compounds are preferentially adsorbed by the carbonate bedrock, while during low input of humic-like compounds, a large portion of the compounds are likely to desorb again from the bedrock (Jin and Zimmerman, 2010). In the presented data set, this process,

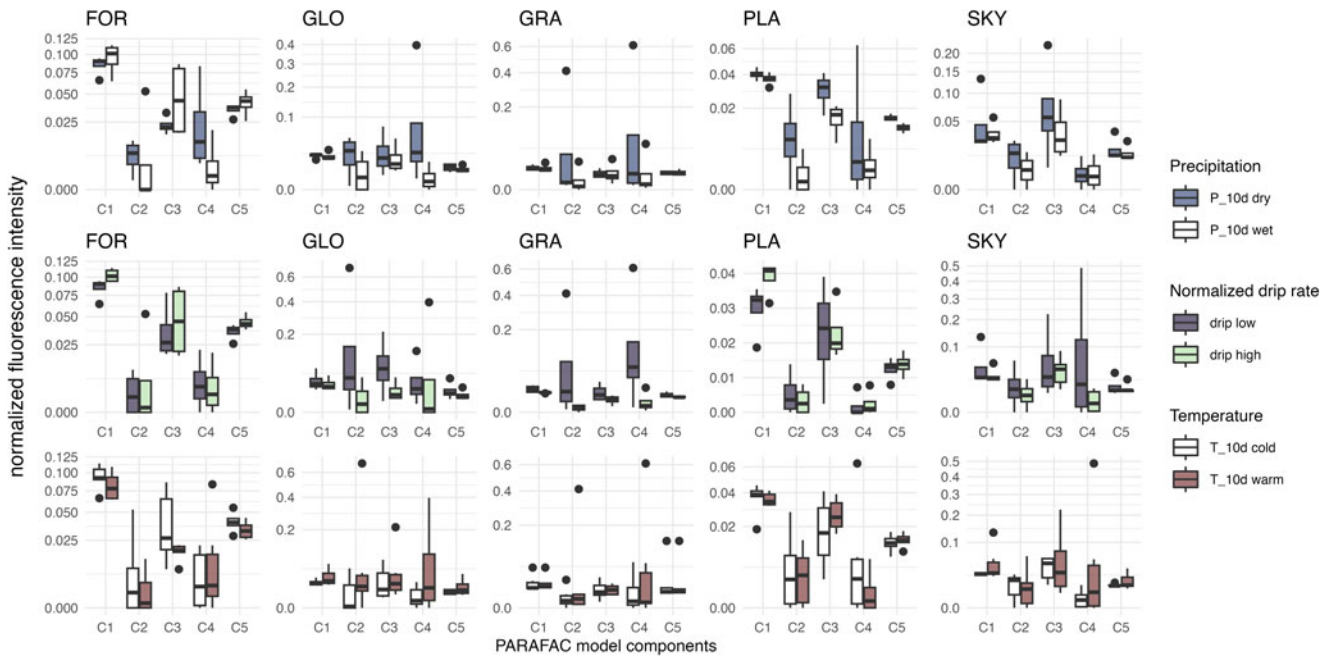


Figure 9. Relationship of climate conditions versus fluorescence intensity of each PARAFAC component for the five locations *FOR*, *GLO*, *GRA*, *PLA*, and *SKY*. In the upper row, data were split in dry or wet conditions based on the total precipitation in the 10 days before sampling. In the middle row, data were split in a high and a low drip rate group, based on the normalized drip rate (previously reported in Kost et al., 2023). The bottom row shows an analogous comparison of warm versus cold average surface temperatures to fluorescence. The sample size of each group ($n=4$) was limited by the total length of the time series of location *FOR*. The boxplots show the median, first, and third quartiles; the attached whiskers extend from the hinges to the extreme values, no farther than $1.5 \times$ inter-quartile range; and data outside of whiskers are plotted as single black dots.

together with the release of indigenous organic matter from bedrock, might have weakened a potential seasonal cycle, leading to basically constant values of humic-like fluorescence at a location such as *FOR*.

In contrast, microbial components C2 and C4 are enhanced for dry conditions across all drip sites. Here, the difference in C4 between the two conditions is more pronounced for shallow locations *FOR* and *GLO*, than for *PLA* and *SKY*. Because all monitored sites continued dripping throughout the 16-month monitoring period, we infer that water is present continually within the karst. However, we hypothesize that the presence of cavities in semi-dry aquifers enhances the conditions for microbial life (C2, C3, C4). Shallow locations might react more readily because they dry out faster and carbon sources for microbes might be more abundant. An alternative interpretation would be that the microbial population and its contributions are diluted during wet periods. Similar results (an increased presence of autochthonous microbial fluorescence for drier conditions) have been found experimentally for karstic subsurface environments (Xia et al., 2022). The groups presented here are too small for statistical tests, but a t-Test on the difference between the means of humic components (C1, C5) and microbial components (C2, C4) over data from all locations yields significantly higher values in dry conditions for microbial components (p -value = 0.021, Supplementary Fig. 3).

The analysis yields similar results if instead of 10-day antecedent rainfall, the normalized drip rate is compared to the PARAFAC components (Fig. 9, middle row). Components C1, C3, and C5 do not show a consistent sign of enhancement or depletion during wet periods across the examined sites. Periods of lower drip rate led to enhanced C2 and C4 in all sites except C4 in *PLA*. Another difference compared to the results for

precipitation is that *PLA* humic-like component C1 is also stronger for higher drip rate.

In contrast to precipitation, with the same methodology, no effect of ambient temperature on the fluorescence fingerprint was detected (Fig. 9, bottom row), which is justified by the constant temperature conditions present within the karst ($T_{\text{mean}} = 13.96^\circ\text{C}$, average seasonal variation with $\text{SD} \pm 32^\circ\text{C}$) (Fig. 9, bottom row).

Relationship of fluorescence to soil respiration, bedrock dissolution, and chelated metal transport

We relate the fluorescence signals to indicators of karst processes measured on the same drip water samples by comparing the PARAFAC model to the carbon isotopic ratio of dissolved inorganic carbon ($\delta^{13}\text{C}_{\text{DIC}}$) and to selected trace elements. The drip water chemistry data in this section have been presented in detail in Kost et al. (2023) and are cited here to highlight the relationship with fluorescence properties. The relationship between the selected fluorescence intensities and drip water chemistry variables is presented graphically in Figure 10 and numerically in Table 3. All correlations in this section are given as Spearman rank correlation coefficients (c_{cor}) because the underlying data distribution is non-parametric.

The $\delta^{13}\text{C}_{\text{DIC}}$ in drip water is interpreted as an indicator of the soil and epikarst CO_2 , which in turn is driven by the aggregate autotrophic and heterotrophic respiration rates (Kost et al., 2023). More negative $\delta^{13}\text{C}_{\text{DIC}}$ indicates higher respiration rates. At the shallow and rapid-transmitting *FOR* location, the higher soil and epikarst respiration rates coincide with the highest concentrations of C1 (and C5), suggesting either that that high respiration rates contribute to high production of humic-like

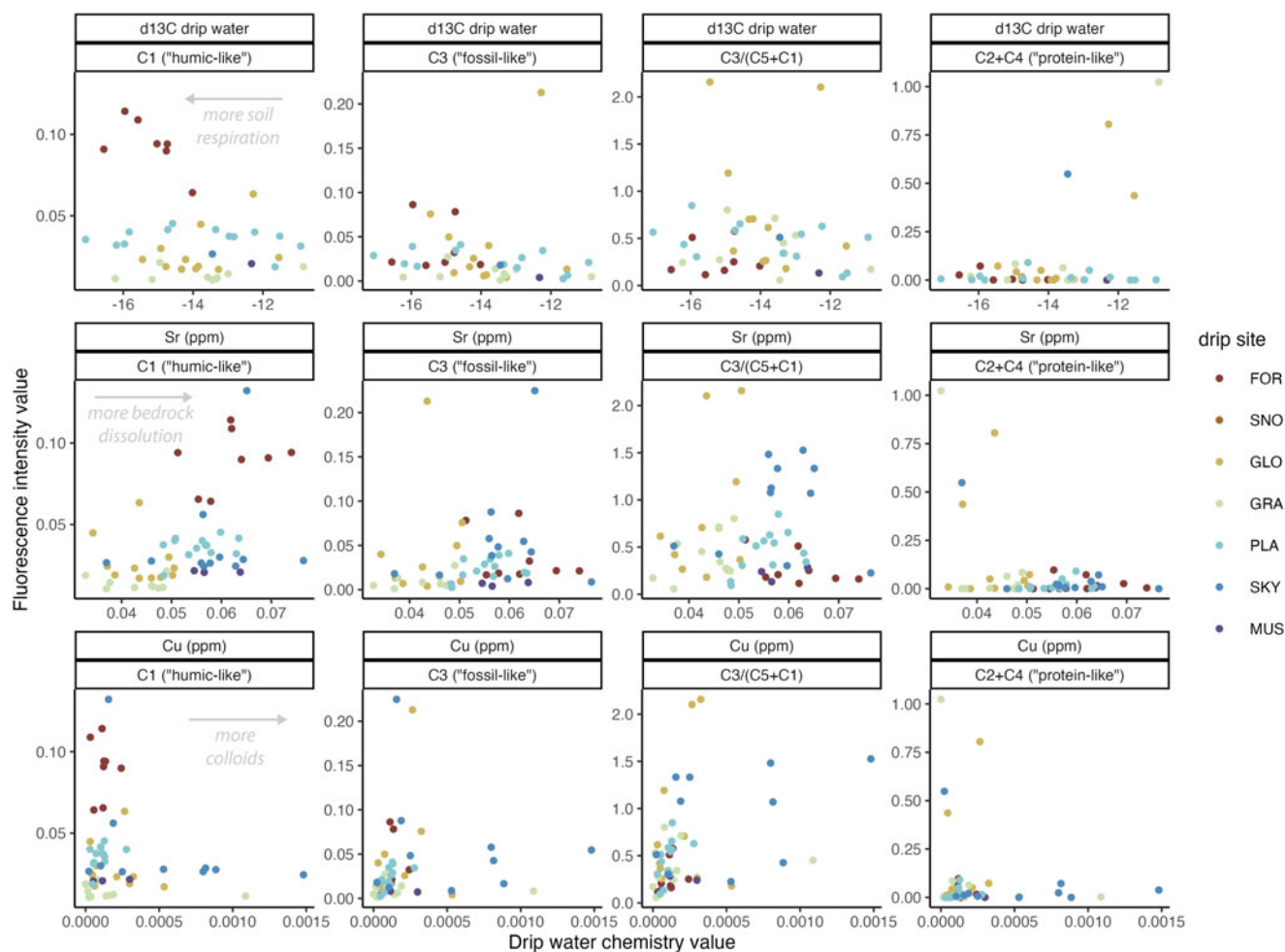


Figure 10. Graphical representation of relationships between fluorescence (C1, C3, C3/(C5+C1), C2+C4) and selected drip water geochemistry parameters. Drip water chemistry data ($\delta^{13}\text{C}_{\text{DIC}}$, Sr concentration, Cu concentration) is re-used from the study Kost et al., 2023. For numerical values of Spearman rank correlation coefficients, see Table 3. **(A)** Comparison of fluorescence with the $\delta^{13}\text{C}$ of DIC in drip water, which is an indicator of soil and epikarst CO_2 and respiration rates. **(B)** Comparison of fluorescence with drip water Sr concentration, which is an indicator of the extent of dissolution of karst bedrock. **(C)** Comparison of fluorescence with the total drip water Cu concentration as an indicator for the presence of colloidal organic complexes.

breakdown products, or that conditions optimal for maximizing respiration are also optimal for maximizing the release of humic-like components to waters (Fig. 10A). We suspect that at the other sites with long data series (SKY, PLA, GLO, GRA), longer water reservoir times may attenuate the seasonal signal in dissolved fluorescence leaving the soil layer relative to the cycle of $\delta^{13}\text{C}_{\text{DIC}}$. This is because $\delta^{13}\text{C}_{\text{DIC}}$ is not sensitive to water residence time when it is set by continued CO_2 exchange with water throughout the infiltration pathway by deep-rooted trees (Breecker et al., 2012). Over the full data set, a significant negative relationship ($c_{\text{cor}} = -0.35$, p -value = 0.03) is present between $\delta^{13}\text{C}_{\text{DIC}}$ and C3. This might be related to active heterotrophic bacteria, which contribute to increased soil respiration and C3-type fluorescence. No further significant relationship was observed between the $\delta^{13}\text{C}_{\text{DIC}}$ and the fraction of fresher versus the more degraded compounds (C3/[C1+C5] ratio) or the concentration of the C2 and C4 compounds, at any site.

In this cave setting, within a given drip site, the concentration of Sr has been proposed as an indicator of the intensity of bedrock dissolution, because all drip water Sr is bedrock sourced and the concentration of Sr is not appreciably affected by precipitation of

CaCO_3 prior to sampling of drip water (Kost et al., 2023). Across all of the sampled sites, there is a general positive monotonic relationship between the Sr concentration and the concentration of C1 ($c_{\text{cor}} = 0.58$, p -value < 0.01), driven primarily by the higher concentrations in the FOR site compared to other sites (Fig. 10B). This correlation may arise because greater soil and epikarst respiration and CO_2 are required to attain greater degrees of bedrock dissolution, and these higher rates of respiration result in greater production of humic-like components. The forested vegetation of the FOR site would especially favor high respiration rates. Similarly, over the entire data set, C3 and bedrock dissolution correlate positively ($c_{\text{cor}} = 0.38$, p -value < 0.01), which would be coherent with increased indigenous fluorescence release in environments of enhanced bedrock dissolution. A similar behavior is observed for Ca concentration, which is interpreted as another proxy for bedrock dissolution (Supplementary Fig. 4).

Highly insoluble transition metals and REE-like elements such as Cu or Y are inferred to be transported in drip waters as complexes with organic ligands such as humic and fulvic acids (Hartland et al., 2014; Hartland and Zitoun, 2018). In stalagmites, seasonal layers of enhanced fluorescence often coincide with

Table 3. Strength of selected monotonic relationships between drip water chemistry (re-used from Kost et al., 2023) and PARAFAC model variables (this study), based on splits of the same drip water samples. The Spearman rank correlation coefficient is given in the top row by location and for the complete data set for each combination. The bottom row (in parentheses) shows the number of joint observations, followed by the p -value. Significant monotonic relationships with p -values < 0.05 appear in bold type. The correlations at *MUS* and *SNO* locations, and between *SKY* and $\delta^{13}\text{C}_{\text{DIC}}$, are not given because fewer than three joint observations between drip water chemistry and the PARAFAC model are available.

Variables	<i>FOR</i>	<i>GLO</i>	<i>GRA</i>	<i>PLA</i>	<i>SKY</i>	full data
$\delta^{13}\text{C}_{\text{DIC}} \alpha$	-0.57	0.21	0.33	-0.13	NA	-0.24
C1	(7, 0.18)	(11, 0.54)	(9, 0.38)	(13, 0.67)		(42, 0.13)
$\delta^{13}\text{C}_{\text{DIC}} \alpha$	-0.14	-0.23	0.17	-0.41	NA	-0.35
C3	(7, 0.76)	(11, 0.84)	(9, 0.67)	(13, 0.17)		(42, 0.03)
$\delta^{13}\text{C}_{\text{DIC}} \alpha$	0.32	-0.38	-0.08	-0.37	NA	-0.13
C3/(C1 + C5)	(7, 0.48)	(11, 0.25)	(9, 0.83)	(13, 0.21)		(42, 0.4)
$\delta^{13}\text{C}_{\text{DIC}} \alpha$	-0.64	0.12	-0.07	-0.22	NA	-0.07
(C2 + C4)	(7, 0.12)	(11, 0.71)	(9, 0.83)	(13, 0.47)		(42, 0.65)
Ca (ppm) α	-0.14	0.08	-0.05	0.16	0.35	0.4
C1	(8, 0.74)	(11, 0.81)	(9, 0.90)	(13, 0.59)	(11, 0.29)	(55, <0.01)
Ca (ppm) α	-0.33	0.25	0.23	0.42	0.17	0.29
C3	(8, 0.42)	(11, 0.47)	(9, 0.55)	(13, 0.15)	(11, 0.61)	(55, 0.03)
Ca (ppm) α	-0.67	0.31	0.45	0.43	0.072	0.005
C3/(C1 + C5)	(8, 0.07)	(11, 0.35)	(9, 0.22)	(13, 0.14)	(11, 0.83)	(55, 0.97)
Ca (ppm) α	0.33	0.35	0.13	0.49	-0.25	0.12
(C2 + C4)	(8, 0.42)	(11, 0.29)	(9, 0.73)	(13, 0.09)	(11, 0.47)	(55, 0.38)
Sr (ppm) α	0.26	-0.37	0.08	0.20	0.3	0.58
C1	(8, 0.53)	(11, 0.26)	(9, 0.83)	(13, 0.53)	(11, 0.36)	(55, <0.01)
Sr (ppm) α	0.02	0.08	0.23	0.43	0.01	0.38
C3	(8, 0.95)	(11, 0.81)	(9, 0.55)	(13, 0.14)	(11, 0.98)	(55, <0.01)
Sr (ppm) α	-0.60	0.22	0.45	0.47	-0.01	0.01
C3/(C1 + C5)	(8, 0.12)	(11, 0.52)	(9, 0.22)	(13, 0.19)	(11, 0.98)	(55, 0.94)
Sr (ppm) α	0.14	0.03	0.13	0.65	-0.27	0.02
(C2 + C4)	(8, 0.74)	(11, 0.94)	(9, 0.73)	(13, 0.02)	(11, 0.42)	(55, 0.8)
Cu (ppm) α	-0.14	-0.36	-0.22	0.23	-0.47	0.01
C1	(8, 0.74)	(10, 0.31)	(9, 0.58)	(13, 0.49)	(10, 0.17)	(53, 0.92)
Cu (ppm) α	0.48	-0.05	0.3	0.71	0.01	0.33
C3	(8, 0.32)	(10, 0.88)	(9, 0.43)	(13, <0.01)	(10, 0.99)	(53, 0.02)
Cu (ppm) α	0.41	0.03	0.43	0.80	0.30	0.39
C3/(C1 + C5)	(8, 0.32)	(10, 0.93)	(9, 0.24)	(13, <0.01)	(10, 0.41)	(53, <0.01)
Cu (ppm) α	0	-0.07	0.1	0.79	-0.07	0.1
(C2 + C4)	(8, 1)	(10, 0.29)	(9, 0.80)	(13, <0.01)	(10, 0.86)	(53, 0.46)
Y (ppm) α	-0.33	-0.31	-0.36	-0.01	-0.62	0.26
C1	(8, 0.42)	(10, 0.38)	(8, 0.39)	(13, 0.99)	(11, 0.04)	(53, 0.06)
Y (ppm) α	-0.29	-0.18	-0.17	0.06	0.51	0.33
C3	(8, 0.49)	(10, 0.63)	(8, 0.69)	(13, 0.85)	(11, 0.11)	(53, 0.01)
Y (ppm) α	-0.52	-0.16	-0.10	0.06	0.71	0.28
C3/(C1 + C5)	(8, 0.18)	(10, 0.65)	(8, 0.82)	(13, 0.85)	(11, 0.02)	(53, 0.72)
Y (ppm) α	0.26	-0.30	0.1	0.23	-0.04	0.05
(C2 + C4)	(8, 0.53)	(10, 0.41)	(8, 0.87)	(13, 0.45)	(11, 0.92)	(53, 0.72)

elevated concentrations of these elements (Borsato et al., 2023; Sliwinski et al., 2023). However, a comparison of C1 and C5 concentrations with the concentration of drip water Cu (Fig. 10C) or Y (Supplementary Fig. 4) reveals no significant correlations within a given site or across all sites. This lack of relationship may have several causes: (1) the signal-to-noise ratio is too low and the time series too short; (2) the Cu and Y concentrations in drip water may be controlled by unique components of the dissolved organic carbon pool than resolved by the C1 or C5 fluorescence, (3) fluorescent DOM present is not necessarily attached to colloids, or (4) other controls of selective scavenging of either Y or organic ligands decouple any initial relationship. Although significant correlations are found in this data set between Cu and C3 ($c_{\text{cor}} = 0.33$, p -value = 0.02), and Cu and C3/(C1+C5) ($c_{\text{cor}} = 0.39$, p -value < 0.01), we argue against interpreting these further due to the heteroscedasticity exposed in Figure 10C. Instead, the precise relationship between Y or transition metals and dissolved organic components in drip waters, which has been mainly explored rigorously in a hyper alkaline cave setting (Hartland et al., 2014), may require further analysis in typical karst settings.

Relating drip water fluorescence and speleothem fluorescence

While the prevailing hypothesis for fluorescent laminae in speleothems invokes an autumnal pulse in fluorescent components (along with colloiddally transported metals) with the onset of autumnal rains and infiltration after a dry summer, our sampling has not detected any seasonal pulses of humic-like or fulvic-like fluorescence in autumn or any other season in the drip water at any monitored sites (Fig. 6), nor did we detect a relationship between C1 or C5 with precipitation at SKY (Fig. 9). In previous studies, fluorescent lamination has been attributed to humic- and fulvic-like components (e.g., McGarry and Baker, 2000; Pearson et al., 2020), although we are aware of no full EEM characterization of the speleothem fluorescence from annually laminated stalagmite samples.

Because of the low concentrations of organic matter, we have not obtained EEM spectra of our actively growing stalagmites, so the conventional inference of humic- and fulvic-like source components of the fluorescent laminae cannot be tested in these active stalagmites. Yet, given the absence of any seasonal variation in humic-like and fulvic-like drip water concentrations at our cave setting, several alternative processes may contribute to the formation of annual to sub-annual fluorescent laminae. Based on our analysis of dissolved fluorescence, the 488 nm excitation wavelength of the CLSM is suitable to stimulate fluorescence in the humic-like and fulvic-like region of C1 or C5. First, if the fluorescent lamina were dominated by the C1 and C5 components, which have constant concentrations in drip water, it is possible that a concentrated fluorescent layer reflects variable dilution of the fluorescence in the stalagmite as a function of the CaCO₃ deposition rate rather than changes in the delivery of fluorescent components. An analogous mechanism has been described for the generation of a seasonal Y peak in stalagmites, whereby periods of slower stalagmite growth distribute an otherwise constant Y (or fluorescence) flux over a shorter distance in the stalagmite, generating higher average concentrations in the slower growth portion of the year (Sliwinski et al., 2023). Based on calculations from the monitored drip water Ca concentrations and the cycle in cave air pCO₂, stalagmite growth at SKY is simulated to occur rapidly during the winter season, and slowly during the summer season, with brief periods of negligible growth

simulated during the spring and fall (Kost et al., 2023). In such a stalagmite growth regime, the slow growth during summer could lead to enhanced fluorescent intensity in the summer layer and weaker fluorescent intensity in the winter layer. An alternative mechanism for the development of a fluorescent lamina could be an increased absorption or trapping efficiency of the fluorescent components in the stalagmite during one season due to changes in factors such as drip water pH or residence time on the stalagmite. Here, further experiments testing the affinity of different organic ligands to Ca and trace elements would be beneficial for interpretation.

In some of our monitored drip waters (GLO, SKY, and to a lesser extent FOR), the C3 component exhibited greater temporal variation than C1 or C5. Although comparing solid state and dissolved fluorescence is not straightforward, we note that the polished bedrock sample, which is dominated by a C3-like component in dissolved form, also indicates pronounced fluorescence, concentrated in certain sectors, by this same 488 nm excitation wavelength in the solid state CLSM analysis of the stalagmites (Fig. 3D). This suggests that this bedrock component, if present without further modification, also would be detected in our stalagmite CLSM analyses. If this component were the main source of fluorescence in the laminae, the variations in C3 concentration in drip water might contribute to modest seasonal variation in speleothem fluorescence. However, the distinct drip water sites exhibited different seasons of maximum C3 fluorescence, so if this were the dominant process behind laminations, it would imply that the bright fluorescent laminae may not represent the same season in all stalagmites from a given cave.

C2 and C4 components exhibit consistent increases during dry intervals, so if these components dominated the variability in the stalagmite laminae, they could contribute to systematic oscillations on annual to sub-annual scales. One caution is that based on our analysis of dissolved fluorescence, the 488 nm excitation wavelength of the CLSM is less suitable to stimulate fluorescence in the C2 or C4 region (C2 Ex_{max} = 265 nm, C4 Ex_{max} = 255 nm). A further caution is that the sites exhibiting significant variations in C2, C3, and C4 components are also in sectors of the cave beneath livestock activity. We cannot assess if such variations would characterize a natural system, or if they are enhanced by the variation in livestock presence. A final possible explanation could be that the fluorescent layers are driven by a season of elevated in-situ microbial production on the stalagmite surface. Lipid distributions document a unique microbial community on the surface of stalagmites that is distinct from soil microbial communities transmitted in drip waters (Blyth et al., 2014, 2016; Lange-Enyedi et al., 2021), but it is not yet known how the microbial density of the stalagmite surface community might vary temporally and affect fluorescence.

We favor explanations related to growth phases as important factors for the generation of annual to sub-annual fluorescent laminae, based on their relevance for also explaining cyclicity in colloiddally transported trace elements. This concept also would be consistent with observations from Ernesto Cave speleothems, in which periods of condensed growth coincide with a higher overall fluorescence (Borsato et al., 2023). The process could also provide an explanation for the lack of annual to sub-annual scale fluorescent lamination in some active stalagmites from the cave (such as PG-2, close to the drip site PLA). At some drip locations, including PLA, stalagmite growth is modeled to occur rapidly but only during one brief part of the year (Kost et al., 2023). In such a case, there may not be variation in the deposition rate of

the formed calcite, and therefore fluorescence incorporation could be homogeneous. Further characterization of the sources of fluorescent components in stalagmites featuring annual lamination will be important to test the alternative hypotheses for layer formation.

Interpretation of fluorescence: implications

These findings have several important implications for the interpretation of fluorescence and fine-scale annual to sub-annual fluorescent lamination in stalagmites. First, the surface vegetation signal of humic-like and fulvic-like fluorescence may dominate the drip water fluorescence signal reaching stalagmites only in settings that feature low water reservoir times and limited microbial reworking. Our data are consistent with a greater reduction in the concentration of fluorescent compounds in very slow-flow drip sites compared to fast-flow drip sites, likely due to the adsorption of fluorescent compounds to host karst rock. Interpretation of the fluorescent components in stalagmites, therefore, needs to consider the reprocessing reactions that operate between the surface environment and the cave. Additionally, a bedrock source of fossil fluorescent material, independent of the surface landscape or climate conditions at the time of stalagmite growth, may be significant in some cave systems, such as ours.

Our finding of annual to sub-annual cyclic fluorescent layers in an actively growing stalagmite beneath a drip characterized by invariant humic- and fulvic-like components challenges one conventional interpretation for the origin of fluorescent laminae by a high autumnal influx of organic matter. Our favored interpretation is that fluorescent laminae could be generated during seasons of slower stalagmite growth in which an otherwise constant concentration of fluorescent components is concentrated over a shorter distance in the stalagmite, generating higher average stalagmite fluorescence in the slower-growth portion of the year. In this case, the season of maximum fluorescence may not be identical among multiple caves or even among multiple stalagmites in the same cave system, because season of stalagmite growth depends on the timing and intensity of cave ventilation, which can vary both among different caves and within a given cave system. Thus, caution should be exercised when generalizing and ascribing the fluorescent laminae consistently to a particular season or to reference a particular season to observed cycles in $\delta^{13}\text{C}$ or trace elements across multiple speleothems and cave systems.

Alternatively, fluorescent laminae could be dominated by variations in the protein-like components of fluorescence. These components (C2, C4) were systematically elevated during dry intervals. If these components are most responsible for fluorescent lamination, then fluorescent laminae may represent dry periods—the opposite interpretation of the conventional hypothesis. In our sites, variations in these components were not synchronous among multiple drip locations, indicating that this process also could lead to seasonally diachronous fluorescent layers in different drip settings. Nonetheless, additional monitoring studies in cave settings with less livestock influence would be important to distinguish if large variations in drip water tyrosine-like and protein-like components also characterize systems in a more natural state. More generally, to reconcile the interpretation of fluorescent laminae in stalagmites with more confidence, it will be important to identify which fluorescent components are responsible for the annual to sub-annual scale lamination in stalagmites by EEM or other analytical approaches. Some fluorescent

components may be selectively incorporated in stalagmite calcite and therefore play a larger role than predicted by their relative contribution to the drip water fluorescence. Further research is needed to assess if the constancy of humic-like and fulvic-like drip water concentrations in this cave are representative of other cave systems in which annual to sub-annual fluorescent laminae are documented.

CONCLUSIONS

This study sought to investigate sources and types of organic matter responsible for fluorescence in speleothems and cave drip waters. This understanding has the potential to provide an additional speleothem proxy to guide paleo-environmental interpretations as well as to improve speleothem age control. To this aim, we have developed and discussed a 5-component parallel factor analysis (PARAFAC) model from a yearlong monitoring of fluorescence in drip water in La Vallina Cave (northern part of the Iberian Peninsula). Additionally, we paired the model to drip water chemistry data previously published in Kost *et al.* (2023) and confocal laser scanning images of actively growing speleothems.

All drip sites show significant organic matter concentrations throughout the year, as indicated by fluorescence measurements, with intensities ranging from 10.88–47.50 R.U. (total fluorescence). The fluorescent organic matter likely originates from the overlying vegetation, sectors of livestock grazing above the cave, microbial processes, and the bedrock. Fluorescence intensity varies significantly among drip sites, with the main drivers being land cover and water reservoir times. Sites with potentially lower residence time, such as *FOR*, show generally higher humic-like fluorescence intensities (C1, C5) and fewer signs of degradation of organic compounds (a low $\text{C3}/[\text{C1}+\text{C5}]$ ratio). Further, the presented evidence suggests that enhanced soil respiration and bedrock dissolution coincide with higher humic-like (C1, C3) fluorescence. In contrast, under long flow routes and reservoir times, drip sites fed by a low water flow may lose a greater fraction of DOM to adsorption on karst host rock, reducing the final concentration arriving at the drip point in the cave (especially C5, Humic C+ fluorescence).

While the prevailing hypothesis for fluorescent laminae in speleothem invokes an autumnal pulse in fluorescent components with heavy infiltration events, our sampling did not detect any seasonal pulses of humic-like fluorescence. Instead, humic-like fluorescence (C1, C5) remained rather constant on a drip-site specific level over the course of the year, whereas the potentially microbially controlled components (C2, C3, C4) showed more variations and increase in concentration during drier periods across all drip sites. Highly insoluble transition metals and REE-like elements such as Cu or Y are expected to be transported in drip waters as complexes (colloids) together with organic ligands, especially during heavy infiltration events. Yet, no robust relationship between these types of compounds and the fluorescence components could be found in our data set.

Overall, these findings have several important implications for the interpretation of fluorescence and fine-scale annual to sub-annual fluorescent laminations in stalagmites: (1) surface vegetation signal of humic-like fluorescence may dominate drip water fluorescence signal, but only in drip sites that feature low water reservoir times and limited microbial reworking; (2) a bedrock source of fossil fluorescent material, independent of the surface landscape or climate conditions at the time of stalagmite growth, may be significant in some cave systems; (3) the evidence

presented here challenges the conventional view of the origin of fluorescent laminae by a high autumnal influx of organic matter; (4) instead of seasonal changes in drip water fluorescence as the dominant control on the formation of stalagmite fluorescent laminations, we favor interpretations that invoke stalagmite surface processes for generating these laminations, and we propose that phases of lower stalagmite growth, in which fluorophores can concentrate in the speleothem over a shorter distance in the year, are a more likely cause of speleothem fluorescent laminations; (5) caution should be applied in this case for layer counting because laminae formation may not be identical across multiple caves or even within multiple stalagmites from the same cave system because stalagmite growth depends on the timing and intensity of cave ventilation, among other factors; (6) the role of microbial processes in the epikarst and within the caves merits further exploration because of the potential effect on the interpretation of fluorescence properties of speleothems.

Competing Interests. The authors declare that they have no known competing interests or personal relationships that could have appeared to influence the work reported in this paper.

Acknowledgments. This study was supported by ETH core funding and ETH Zürich (grant number ETH-1318-1). We would like to thank Jacqueline Traber from EAWAG for discussion and tests of techniques and enabling the collaboration. We thank Kathleen Murphy for discussion of PARAFAC models. We acknowledge the constructive suggestions of Andrea Borsato and an anonymous reviewer in improving the structure of the manuscript.

Data and code availability. The codes for reproducing the plots are available on GitHub (https://github.com/lrndrs/Fluorescence_LaVallina_QR; last access: 4 July 2023). A compiled drip water organics and chemistry data set is available in the supplementary and on PANGAEA (<https://www.pangaea.de/>; last access: 30 December 2022), and the PARAFAC model is published in the OpenFluor database (<https://openfluor.lablicate.com>; last access: 4 July 2023).

REFERENCES

- AEMET, 2011. *Atlas Climático Ibérico – Iberian Climate Atlas*. <https://doi.org/10.31978/784-11-002-5>.
- AEMET, 2021. *State Meteorological Agency of Spain open data*. <http://www.aemet.es/en/portada>. [accessed 13 September 2021]
- Aiken, G.R., 2014. Fluorescence and dissolved organic matter: a chemist's perspective. In: Coble, P., Lead, J., Baker, A., Reynolds, D., Spencer, R. (Eds.), *Aquatic Organic Matter Fluorescence* (Cambridge Environmental Chemistry Series). Cambridge University Press, Cambridge, UK, pp. 35–74.
- Alberts, J.J., Takács, M., 2004. Comparison of the natural fluorescence distribution among size fractions of terrestrial fulvic and humic acids and aquatic natural organic matter. *Organic Geochemistry* **35**, 1141–1149.
- Álvarez, R., Ordóñez, A., Canteli, P., De Miguel, E., 2019. Unconventional gas resources in the Cantabrian Zone (NW Spain): a comprehensive preliminary assessment. *Geological Journal* **54**, 2608–2620.
- Baker, A., Genty, D., 1999. Fluorescence wavelength and intensity variations of cave waters. *Journal of Hydrology* **217**, 19–34.
- Baker, A., Smart, P.L., Edwards, R.L., Richards, D.A., 1993. Annual growth banding in a cave stalagmite. *Nature* **364**, 518–520.
- Baker, A., Elliott, S., Lead, J.R., 2007. Effects of filtration and pH perturbation on freshwater organic matter fluorescence. *Chemosphere* **67**, 2035–2043.
- Baker, A., Smith, C., Jex, C., Fairchild, I., Genty, D., Fuller, L., 2008. Annually laminated speleothems: a review. *International Journal of Speleology* **37**, 193–206.
- Birdwell, J.E., Engel, A.S., 2010. Characterization of dissolved organic matter in cave and spring waters using UV–Vis absorbance and fluorescence spectroscopy. *Organic Geochemistry* **41**, 270–280.
- Blyth, A.J., Baker, A., Collins, M.J., Penkman, K.E.H., Gilmour, M.A., Moss, J.S., Genty, D., Drysdale, R.N., 2008. Molecular organic matter in speleothems and its potential as an environmental proxy. *Quaternary Science Reviews* **27**, 905–921.
- Blyth, A.J., Jex, C.N., Baker, A., Khan, S.J., Schouten, S., 2014. Contrasting distributions of glycerol dialkyl glycerol tetraethers (GDGTs) in speleothems and associated soils. *Organic Geochemistry* **69**, 1–10.
- Blyth, A.J., Hartland, A., Baker, A., 2016. Organic proxies in speleothems—new developments, advantages and limitations. *Quaternary Science Reviews* **149**, 1–17.
- Borsato, A., Frisia, S., Fairchild, I.J., Somogyi, A., Susini, J., 2007. Trace element distribution in annual stalagmite laminae mapped by micrometer-resolution X-ray fluorescence: implications for incorporation of environmentally significant species. *Geochimica et Cosmochimica Acta* **71**, 1494–1512.
- Borsato, A., Fairchild, I.J., Frisia, S., Wynn, P.M., Fohlmeister, J., 2023. The Ernesto Cave, northern Italy, as a candidate auxiliary reference section for the definition of the Anthropocene Series. *The Anthropocene Review* **10**, 269–287.
- Bosch, J.M., Hewlett, J.D., 1982. A review of catchment experiments to determine the effect of vegetation changes on water yield and evapotranspiration. *Journal of Hydrology* **55**, 3–23.
- Breecker, D.O., Payne, A.E., Quade, J., Banner, J.L., Ball, C.E., Meyer, K.W., Cowan, B.D., 2012. The sources and sinks of CO₂ in caves under mixed woodland and grassland vegetation. *Geochimica et Cosmochimica Acta* **96**, 230–246.
- Bro, R., Kiers, H.A.L., 2003. A new efficient method for determining the number of components in PARAFAC models. *Journal of Chemometrics* **17**, 274–286.
- Carracedo, V., Cunill, R., García-Codron, J.C., Pélachs, A., Pérez-Obiol, R., Soriano, J.M., 2018. History of fires and vegetation since the Neolithic in the Cantabrian Mountains (Spain). *Land Degradation & Development* **29**, 2060–2072.
- Carrión, Y., Kaal, J., López-Sáez, J.A., López-Merino, L., Martínez Cortizas, A., 2010. Holocene vegetation changes in NW Iberia revealed by anthracological and palynological records from a colluvial soil. *The Holocene* **20**, 53–66.
- Chen, M., Jung, J., Lee, Y.K., Hur, J., 2018. Surface accumulation of low molecular weight dissolved organic matter in surface waters and horizontal off-shelf spreading of nutrients and humic-like fluorescence in the Chukchi Sea of the Arctic Ocean. *Science of the Total Environment* **639**, 624–632.
- Coble, P.G., Spencer, R.G.M., Baker, A., Reynolds, D.M., 2014. Aquatic organic matter fluorescence. In: Coble, P.G., Lead, J., Baker, A., Reynolds, D.M., Spencer, R.G.M. (Eds.), *Aquatic Organic Matter Fluorescence* (Cambridge Environmental Chemistry Series). Cambridge University Press, Cambridge, UK, pp. 75–122.
- Cory, R.M., McKnight, D.M., 2005. Fluorescence spectroscopy reveals ubiquitous presence of oxidized and reduced quinones in dissolved organic matter. *Environmental Science and Technology* **39**, 8142–8149.
- Cramer, F., Shephard, G.E., Heron, P.J., 2020. The misuse of colour in science communication. *Nature Communications* **11**, 5444. <https://doi.org/10.1038/s41467-020-19160-7>.
- Dandrilli, J., McConnell, J.R., 2021. Polar ice core organic matter signatures reveal past atmospheric carbon composition and spatial trends across ancient and modern timescales. *Journal of Glaciology* **67**, 1028–1042.
- Delavaud, E., Cotton, F., Akkar, S., Scherbaum, F., Danciu, L., Beauval, C., Drouet, S., et al., 2012. Toward a ground-motion logic tree for probabilistic seismic hazard assessment in Europe. *Journal of Seismology* **16**, 451–473.
- Elliott, S., Lead, J.R., Baker, A., 2006. Thermal quenching of fluorescence of freshwater, planktonic bacteria. *Analytica Chimica Acta* **564**, 219–225.
- Fairchild, I.J., Baker, A., 2012. *Speleothem Science: From Process to Past Environments*. John Wiley & Sons, Hoboken, New Jersey.
- Ferrere, P., Lopez, G.A., Boca, R.T., Galetti, M.A., Esparrach, C.A., Pathauer, P.S., 2005. Initial density effect on *Eucalyptus globulus* growth in a Nelder modified trial. *Forest Systems* **14**, 174–184.
- Ferreto, D.O.C., Reichert, J.M., Cavalcante, R.B.L., Srinivasan, R., 2021. Water budget fluxes in catchments under grassland and *Eucalyptus* plantations of different ages. *Canadian Journal of Forest Research* **51**, 513–523.
- Gabor, R.S., McKnight, D.M., Miller, M.P., 2014. Fluorescence indices and their interpretation. In: Coble, P.G., Lead, J., Baker, A., Reynolds, D.M.,

- Spencer, R.G.M. (Eds.), *Aquatic Organic Matter Fluorescence* (Cambridge Environmental Chemistry Series). Cambridge University Press, Cambridge, UK, pp. 303–338.
- Hartland, A., Zitoun, R., 2018. Transition metal availability to speleothems controlled by organic binding ligands. *Geochemical Perspectives Letters* **8**, 22–25.
- Hartland, A., Fairchild, I.J., Müller, W., Dominguez-Villar, D., 2014. Preservation of NOM-metal complexes in a modern hyperalkaline stalagmite: implications for speleothem trace element geochemistry. *Geochimica et Cosmochimica Acta* **128**, 29–43.
- Heeb, B., 2009. An all-in-one electronic cave surveying device. *Cave Radio and Electronics Group Journal* **72**, 8–10.
- Heeb, B., 2010. A general calibration algorithm for 3-axis compass/clinometer devices. *Cave Radio and Electronics Group Journal* **73**. <https://paperless.bheeb.ch/download/Calibration.pdf>.
- Helms, J.R., Stubbins, A., Ritchie, J.D., Minor, E.C., Kieber, D.J., Mopper, K., 2008. Absorption spectral slopes and slope ratios as indicators of molecular weight, source, and photobleaching of chromophoric dissolved organic matter. *Limnology and Oceanography* **53**, 955–969. [Erratum: <https://doi.org/10.4319/lo.2009.54.3.1023>]
- Huang, Y., Fairchild, I.J., Borsato, A., Frisia, S., Cassidy, N.J., McDermott, F., Hawkesworth, C.J., 2001. Seasonal variations in Sr, Mg and P in modern speleothems (Grotta di Ernesto, Italy). *Chemical Geology* **175**, 429–448.
- IAEA/WMO (International Atomic Energy Agency/World Meteorological Organization), 2022. *Global Network of Isotopes in Precipitation. The GNIP Database*. <https://www.iaea.org/services/networks/gnip>.
- Jin, J., Zimmerman, A.R., 2010. Abiotic interactions of natural dissolved organic matter and carbonate aquifer rock. *Applied Geochemistry* **25**, 472–484.
- Kost, O., González-Lemos, S., Rodríguez-Rodríguez, L., Sliwinski, J., Endres, L., Haghypour, N., Stoll, H., 2023. Relationship of seasonal variations in drip water $\delta^{13}\text{C}_{\text{DIC}}$, $\delta^{18}\text{O}$, and trace elements with surface and physical cave conditions of La Vallina Cave, NW Spain. *Hydrology and Earth System Sciences* **27**, 2227–2255.
- Kwocien, O., Braun, T., Brunello, C.F., Faulkner, P., Hausmann, N., Helle, G., Hoggarth, J.A., et al., 2022. What we talk about when we talk about seasonality – a transdisciplinary review. *Earth-Science Reviews* **225**, 103843. <https://doi.org/10.1016/j.earscirev.2021.103843>.
- Lakowicz, J.R., 2006. *Principles of Fluorescence Spectroscopy*. Springer, New York.
- Lange-Enyedi, N.T., Németh, P., Borsodi, A.K., Halmy, R., Czuppon, G., Kovács, I., Leél-Össy, S., Demény, A., Makk, J., 2021. Calcium carbonate precipitating cultivable bacteria from different speleothems of karst caves. *Geomicrobiology Journal* **39**, 107–122.
- Lechleitner, F.A., Dittmar, T., Baldini, J.U.L., Pruffer, K.M., Eglinton, T.I., 2017. Molecular signatures of dissolved organic matter in a tropical karst system. *Organic Geochemistry* **113**, 141–149.
- Lindeman, I., Hansen, M., Scholz, D., Breitenbach, S.F.M., Hartland, A., 2021. Effects of organic matter complexation on partitioning of transition metals into calcite: cave-analogue crystal growth experiments. *Geochimica et Cosmochimica Acta* **317**, 118–137.
- Luetscher, M., Moseley, G.E., Festi, D., Hof, F., Edwards, R.L., Spötl, C., 2021. A last interglacial speleothem record from the Sieben Hengste cave system (Switzerland): implications for alpine paleovegetation. *Quaternary Science Reviews* **262**, 106974. <https://doi.org/10.1016/j.quascirev.2021.106974>.
- Massicotte, P., 2019. eemR: tools for pre-processing emission-excitation-matrix (EEM) fluorescence data. *R package version 1*(1). <https://cran.r-project.org/web/packages/eemR/index.html>.
- McGarry, S.F., Baker, A., 2000. Organic acid fluorescence: applications to speleothem palaeoenvironmental reconstruction. *Quaternary Science Reviews* **19**, 1087–1101.
- McKnight, D.M., Boyer, E.W., Westerhoff, P.K., Doran, P.T., Kulbe, T., Andersen, D.T., 2001. Spectrofluorometric characterization of dissolved organic matter for indication of precursor organic material and aromaticity. *Limnology and Oceanography* **46**, 38–48.
- Moreno, A., Iglesias, M., Azorín-Molina, C., Pérez-Mejías, C., Bartolomé, M., Sancho, C., Stoll, H., et al., 2021. Measurement report: spatial variability of northern Iberian rainfall stable isotope values – investigating climatic controls on daily and monthly timescales. *Atmospheric Chemistry and Physics Discussions*. <https://doi.org/10.5194/acp-21-10159-2021>.
- Mudarra, M., Andreo, B., Baker, A., 2011. Characterisation of dissolved organic matter in karst spring waters using intrinsic fluorescence: relationship with infiltration processes. *Science of the Total Environment* **409**, 3448–3462.
- Murphy, K.R., Stedmon, C.A., Wenig, P., Bro, R., 2014. OpenFluor—an online spectral library of auto-fluorescence by organic compounds in the environment. *Analytical Methods* **6**, 658–661.
- O'Brien, B.J., 1956. 'After-glow' of cave calcite. *Bulletin of the National Speleological Society* **18**, 50–51.
- Ohno, T., 2002. Fluorescence inner-filtering correction for determining the humification index of dissolved organic matter. *Environmental Science and Technology* **36**, 742–746.
- Öncel, Ş., Uzun, L., Garipcan, B., Denizli, A., 2005. Synthesis of phenylalanine-containing hydrophobic beads for lysozyme adsorption. *Industrial and Engineering Chemistry Research* **44**, 7049–7056.
- Orland, I.J., Bar-Matthews, M., Ayalon, A., Matthews, A., Kozdon, R., Ushikubo, T., Valley, J.W., 2012. Seasonal resolution of Eastern Mediterranean climate change since 34 ka from a Soreq Cave speleothem. *Geochimica et Cosmochimica Acta* **89**, 240–255.
- Pearson, A.R., Hartland, A., Frisia, S., Fox, B.R.S., 2020. Formation of calcite in the presence of dissolved organic matter: partitioning, fabrics and fluorescence. *Chemical Geology* **539**, 119492. <https://doi.org/10.1016/j.chemgeo.2020.119492>.
- Perrette, Y., Delannoy, J.J., Desmet, M., Lignier, V., Destombes, J.L., 2005. Speleothem organic matter content imaging. The use of a fluorescence index to characterise the maximum emission wavelength. *Chemical Geology* **214**, 193–208.
- Philibert, M., Luo, S., Moussanas, L., Yuan, Q., Filloux, E., Zraick, F., Murphy, K.R., 2022. Drinking water aromaticity and treatability is predicted by dissolved organic matter fluorescence. *Water Research* **220**, 118592. <https://doi.org/10.1016/j.watres.2022.118592>.
- Proctor, C.J., Baker, A., Barnes, W.L., Gilmour, M.A., 2000. A thousand year speleothem proxy record of North Atlantic climate from Scotland. *Climate Dynamics* **16**, 815–820.
- Pucher, M., Wünsch, U., Weigelhofer, G., Murphy, K., Hein, T., Graeber, D., 2019. StaRDom: versatile software for analyzing spectroscopic data of dissolved organic matter in R. *Water (Switzerland)* **11**, 2366. <https://doi.org/10.3390/w11112366>.
- Quiers, M., Perrette, Y., Chalmin, E., Fanget, B., Poulenard, J., 2015. Geochemical mapping of organic carbon in stalagmites using liquid-phase and solid-phase fluorescence. *Chemical Geology* **411**, 240–247.
- Ramseier, K., Miano, T.M., D'Orazio, V., Wildberger, A., Wagner, T., Geister, J., 1997. Nature and origin of organic matter in carbonates from speleothems, marine cements and coral skeletons. *Organic Geochemistry* **26**, 361–378.
- Reynolds, D.M., 2014. The Principles of Fluorescence. In: Coble, P.G., Lead, J., Baker, A., Reynolds, D.M., Spencer, R.G.M. (Eds.), *Aquatic Organic Matter Fluorescence* (Cambridge Environmental Chemistry Series). Cambridge University Press, Cambridge, UK, pp. 3–34.
- Rutledge, H., Baker, A., Marjo, C.E., Andersen, M.S., Graham, P.W., Cuthbert, M.O., Rau, G.C., et al., 2014. Dripwater organic matter and trace element geochemistry in a semi-arid karst environment: implications for speleothem paleoclimatology. *Geochimica et Cosmochimica Acta* **135**, 217–230.
- Rutledge, H., Andersen, M.S., Baker, A., Chinu, K.J., Cuthbert, M.O., Jex, C.N., Marjo, C.E., Markowska, M., Rau, G.C., 2015. Organic characterisation of cave drip water by LC-OCD and fluorescence analysis. *Geochimica et Cosmochimica Acta* **166**, 15–28.
- Schindelin, J., Arganda-Carreras, I., Frise, E., Kaynig, V., Longair, M., Pietzsch, T., Preibisch, S., et al., 2012. Fiji: an open-source platform for biological-image analysis. *Nature Methods* **9**, 676–682.
- Shopov, Y.Y., Ford, D.C., Schwarcz, H.P., 1994. Luminescent microbanding in speleothems: high-resolution chronology and paleoclimate. *Geology* **22**, 407–410.
- Sliwinski, J.T., Stoll, H.M., 2021. Combined fluorescence imaging and LA-ICP-MS trace element mapping of stalagmites: microfabric identification

- and interpretation. *Chemical Geology* **581**, 120397. <https://doi.org/10.1016/j.chemgeo.2021.120397>.
- Sliwinski, J.T., Kost, O., Endres, L., Iglesias, M., Hahipour, N., González-Lemos, S., Stoll, H.M.**, 2023. Exploring soluble and colloiddally transported trace elements in stalagmites: the strontium-yttrium connection. *Geochimica et Cosmochimica Acta* **343**, 64–83.
- Spangenberg, M., Bryant, J.I., Gibson, S.J., Mousley, P.J., Ramachers, Y., Bell, G.R.**, 2021. Ultraviolet absorption of contaminants in water. *Scientific Reports* **11**, 3682. <https://doi.org/10.1038/s41598-021-83322-w>.
- Stedmon, C.A., Bro, R.**, 2008. Characterizing dissolved organic matter fluorescence with parallel factor analysis: a tutorial. *Limnology and Oceanography Methods* **6**, 572–579.
- Stedmon, C.A., Cory, R.M.**, 2014. Biological origins and fate of fluorescent dissolved organic matter in aquatic environments. In: Coble, P.G., Lead, J., Baker, A., Reynolds, D.M., Spencer, R.G.M. (Eds.), *Aquatic Organic Matter Fluorescence* (Cambridge Environmental Chemistry Series). Cambridge University Press, Cambridge, UK, pp. 278–300.
- Stedmon, C.A., Markager, S., Bro, R.**, 2003. Tracing dissolved organic matter in aquatic environments using a new approach to fluorescence spectroscopy. *Marine Chemistry* **82**, 239–254.
- Stoll, H., Mendez-Vicente, A., Gonzalez-Lemos, S., Moreno, A., Cacho, I., Cheng, H., Edwards, R.L.**, 2015. Interpretation of orbital scale variability in mid-latitude speleothem $\delta^{18}\text{O}$: significance of growth rate controlled kinetic fractionation effects. *Quaternary Science Reviews* **127**, 215–228.
- Wilkinson, K.J., Nègre, J.-C., Buffie, J.**, 1997. Contaminant hydrology coagulation of colloidal material in surface waters: the role of natural organic matter. *Journal of Contaminant Hydrology* **26**, 229–243.
- Wünsch, U.J., Murphy, K.R., Stedmon, C.A.**, 2015. Fluorescence quantum yields of natural organic matter and organic compounds: implications for the fluorescence-based interpretation of organic matter composition. *Frontiers in Marine Science* **2**. <https://doi.org/10.3389/fmars.2015.00098>.
- Xia, F., Liu, Z., Zhao, M., Li, Q., Li, D., Cao, W., Zeng, C., et al.**, 2022. High stability of autochthonous dissolved organic matter in karst aquatic ecosystems: evidence from fluorescence. *Water Research* **220**, 118723. <https://doi.org/10.1016/j.watres.2022.118723>.
- Yamashita, Y., Jaffé, R.**, 2008. Characterizing the interactions between trace metals and dissolved organic matter using excitation-emission matrix and parallel factor analysis. *Environmental Science and Technology* **42**, 7374–7379.
- Zhou, Z., Guo, L., Shiller, A.M., Lohrenz, S.E., Asper, V.L., Osburn, C.L.**, 2013. Characterization of oil components from the Deepwater Horizon oil spill in the Gulf of Mexico using fluorescence EEM and PARAFAC techniques. *Marine Chemistry* **148**, 10–21.